INVESTIGATION OF THE EFFECT OF CRYSTAL THICKNESS ON THE SPATIAL RESOLUTION AND LINEARITY OF A PEM DETECTOR USING AN ARTIFICIAL NEURAL NETWORK BASED POSITIONING ALGORITHM

by

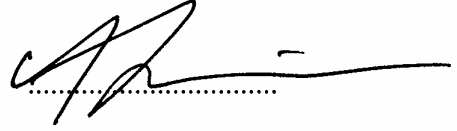## DİDAR TALAT

B.S., Physics, Boğaziçi University, 2005

Submitted to the Institute of Biomedical Engineering
in partial fulfillment of the requirements
for the degree of
Master of Science
in
Biomedical Engineering
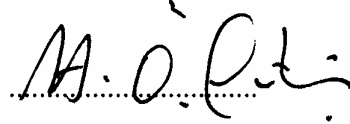
Boğaziçi University
September 2007

INVESTIGATION OF THE EFFECT OF CRYSTAL THICKNESS ON THE SPATIAL RESOLUTION AND LINEARITY OF A PEM DETECTOR USING AN ARTIFICIAL NEURAL NETWORK BASED POSITIONING ALGORITHM
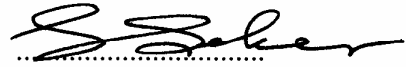
APPROVED BY:

Assoc. Prof. Dr. Albert GÜVENİŞ

(Thesis Advisor)

Assoc. Prof. Dr. H. Özcan GÜLÇÜR

Prof. Dr. Selim ŞEKER

DATE OF APPROVAL: 03.09.2007

ACKNOWLEDGMENTS

ABSTRACT
INVESTIGATION OF THE EFFECT OF CRYSTAL THICKNESS ON THE SPATIAL RESOLUTION AND LINEARITY OF A PEM DETECTOR USING AN ARTIFICIAL NEURAL NETWORK BASED POSITIONING ALGORITHM

The objective of this thesis is to improve the resolution and linearity of a continuous detector for positron emission mammography (PEM) imaging, by using an algorithm based on artificial neural networks. Another aim of this work is to investigate the effect of crystal thickness on the resolution and bias of the detector. A continuous scintillation detector is chosen, in order to overcome the difficulties observed in light collection and manufacturing of pixellated crystals and to reduce the cost.

In this study, the detector is composed of 49 mm x 49 mm continuous LSO crystal where its thickness changes from 3 mm to 24 mm with increments of 3 mm. The photosensor chosen is Hamamatsu H8500 flat panel multi-anode photomultiplier consisting of 8 x 8 anodes. The interactions of narrow beams of 511 keV photons impacting the detector surface and the photosensor output are simulated using DETECT2000 simulation platform. The 64 outputs of the PMT is reduced to 4 and these outputs are used as the input vectors of the multilayer perceptron network for each interaction. Two sets of simulations are performed for each thickness of the scintillation crystal. One set to generate the training set and another set to create the test set. By fixing the parameters of the network and the number of iterations, the effect of crystal thickness and energy threshold on the intrinsic spatial resolution and bias are investigated. Our simulations confirmed the bias problem of the Anger algorithm and the necessity of using a biasfree positioning algorithm for scintillation coordinate estimation.

Using artificial network based positioning algorithm better results are observed when compared to Anger algorithm. Results obtained show an intrinsic resolution of 0.329 mm and 0.690 mm for a crystal thickness of 3 mm and 24 mm in the center of the crystal,

respectively. The systematic errors calculated are better than those obtained with Anger algorithm.

Keywords: Positron emission mammography (PEM), continuous scintillation crystal, positioning algorithm, artificial neural networks, Anger algorithm.

ÖZET

KRİSTAL KALINLIĞININ PEM DETEKTÖRÜNÜN UZAMSAL ÇÖZÜNÜRLÜĞÜNE VE DOĞRUSALLIĞA ETKİSİNİN YAPAY SİNİR AĞLARI TEMELLİ BİR POZİSYONLAMA ALGORİTMASI KULLANILARAK ARAŞTIRILMASI

Bu tezin amacı, sürekli bir PEM detektörünün çözünülürlüğünün ve doğrusallığının yapay sinir ağları temelli bir pozisyonlama algoritması kullanılarak araştırılmasıdır. Bu çalışmanın diğer bir amacı da kristal kalınlığının, çözünürlük ve detektörün sistematik hatasına olan etkisinin incelenmesidir. Bu çalışmada pikselleştirilmiş kristallerin ışık toplamadaki sorunlarının ve işçiliklerindeki zorlukların üstesinden gelmek ve maliyeti azaltmak amacıyla sürekli bir kristal seçilmiştir.

Bu çalışmada kullanılan sürekli LSO kristali, 49 mm x 49 mm boyutlarında olup, kalınlığı 3 mm'den başlanılarak her simülasyon grubu için 3'er mm'lik artırımlarla 24 mm'ye kadar çıkarılmıştır. Seçilen ışık algılayıcı, düz panelli ve 8 x 8 anotlu Hamamatsu H8500'dür. 511 keV enerjili fotonlar dar aşınlar halinde detektörün yüzeyine gönderilmiştir ve kistalin içinde gerçekleşen etkileşimler ve ışık algılayıcının çıkışları simüle edilmiştir. Foton çoğaltıcı tüpün 64 adet çıkışı 4 çıkışa düşürülmüştür ve bu çıkışlar, her etkileşim için çok katmanlı algılayıcının giriş vektörleri olarak kullanılmıştır. Her kristal kalınlığı için biri eğitim, diğeri test setini oluşturmak üzere için iki grup simülasyon gerçekleştirilmiştir. Ağın parametreleri ve ağı eğitmekte kullanılan döngü sayısı her kalınlık için sabit tutularak, kristal kalınlığının ve enerji eşiğinin, detektörün iç çözünürlüğüne ve sistematik hatasına etkisi araştırılmıştır. Yapılan simülasyonlar, Anger algoritmasının sistematik hatasını kanıtlamış ve sintilasyon koordinatı hesaplaması için yanlılık hatası olmayan başka bir pozisyonlama algoritmasının kullanılmasının gerekliliğini kanıtlamıştır.

Yapay sinir ağları temelli bir pozisyonlama algoritması kullanılması Anger algoritmasına kıyasla daha iyi sonuçlar vermiştir. 3 mm kalınlığındaki LSO kristali için merkezdeki çözünürlük 0.329 mm olarak bulunmuştur, kristal kalınlığı 24 mm'ye

çıkarıldığında ise çözünürlük 0.690 mm'ye yükselmiştir. Yanlılık hata değerleri ise Anger algoritması ile hesaplananlardan daha iyidir.

Anahtar Sözcükler: Pozitron emisyon mamografisi (PEM), sürekli sintilasyon kristali, pozisyonlama algoritması, yapay sinir ağları, Anger algoritması.

TABLE OF CONTENTS

LIST OF FIGURES

LIST OF TABLES

LIST OF SYMBOLS

e^-	Electron
e^+	Poistron
$\beta+$	Positron emission
γ	Photon
ν_e	Neutrino
E	Energy
E_{max}	Maximum energy
A(t)	Activity at time t
$T_{1/2}$	Half-life
m	Mass
m_e	Mass of electron
m_p	Mass of proton
c	Speed of light
d	Distance
Δt	Time difference
h	Planck's constant
σ	Interaction cross-section for Compton scattering
τ	Interaction cross-section for photoelectric interaction
κ	Interaction cross-section for pair production
Z	Atomic number
$h\nu$	Photon energy
$h\nu'$	Final photon energy
θ	Angle
$d\Omega$	Infinitesimal solid angle
r_e	Classical electron radius
I_0	Initial intensity
I_x	Intensity measured through a thickness of x
μ	Linear attenuation coefficient
$R_{corr,0}$	Count rate with no attenuation
N	Average number of light photons

Δ_{nc}	Blurring effect coming from colinearity
D	Diameter of a PET scanner
δp	Parallax shift
ω	Weight coefficient
Δz	Difference in depth
V_i	Signal amplitude of ith photosensor
x_{est}	Estimated x coordinate
y_{est}	Estimated y coordinate
b	Bias
$\varphi(.)$	Activation function
x_i	Input of ith neuron
y_i	Output of ith neuron
v_i	Induced local field of ith neuron
n	Number of iterations
e_i	Error signal of ith neuron
ε	Total error energy
ε_{av}	Averaged squared error energy
η	Learning rate parameter
δ_i	Local gradient of ith neuron
$\Delta\omega$	Weight correction

LIST OF ABBREVIATIONS

PEM	Positron emission mammography
PET	Positron emission tomography
SPECT	Single photon emission computed tomography
MRI	Magnetic resonance imaging
FDG	Fluorodeoxyglucose
BGO	Bismuth germinate
GSO	Gadolinium oxyorthosilicate
eV	Electron Volt
J	Joule
PSF	Point spread function
FWHM	Full-width-at-half-maximum
FWTM	Full-width-at-tenth-maximum
PMT	Photomultiplier tube
PD	Photo diode
APD	Avalanche photo diode
PSPMT	Position-sensitive photomultiplier tube
MCPMT	Multi-channel photomultiplier tube
MAPMT	Multi-anode photomultiplier tube
DOI	Depth of interaction
LOR	Line of response
LUT	Look-up-table
ML	Maximum likelihood
UFOV	Useful field-of-view
LRF	Light-response-function
PSAPD	Position-sensitive avalanche photo diode
ANN	Artificial neural network
FOV	Field-of-view
LSO	Lutetium oxyorthosilicate
NaI(Tl)	Thalium doped sodium iodide
BPET	Breast-only positron emission tomography imager

PSF	Point spread function
LSF	Line spread function
PEMT	PEM tomography
AOR	Axis of rotation
MaxPET	Mammary and axillary region PET
LuAP	Lutetium aluminum perovskite
LYSO	Lutetium yttrium orthosilicate
EM	Expectation maximization
YAP	Yttrium aluminium perovskite
SNR	Signal-to-noise ratio
TRIUMF	Tri-University Meson Facility
GRIT	Gamma ray interaction tracking
PDF	Probability density function
VLSI	Very-large-scale-integration
MLP	Multilayer perceptron
LMS	Least-mean-square

1. INTRODUCTION

Breast cancer is the leading cancer and the second leading cause of mortality in women, although the mortality rate from breast cancer has declined through mammographic screening of large segments of the population. Despite these advances, the considerably mortality and morbidity associated with breast cancer necessitates a formidable challenge in this area.

According to the population-based studies, the screening sensitivity of X-ray mammography did not exceed 80% in any segment of the population studied and results in a considerable number of missed cancers, especially in women with dense breasts. The study of Mendelson *et al.* revealed sensitivities for breast cancer detection of 80%, 59%, and 30% in women with predominantly fatty breast tissue, those with heterogeneously dense, and those with extremely dense breasts. It is concluded that breast density is one of the strongest predictors of the failure of mammographic screening to detect cancer. Moreover, Boyd *et al.* found that women with dense breasts are at a 4 to 6 times higher risk of developing breast cancer than those with predominantly fatty breasts. Other reasons for missed breast cancers included misinterpretation of the mammograms, overlooked cancers, and suboptimal technique.

A second important limitation of mammography is its low specificity. That is, the majority (60% to 80%) of breast biopsies reveal benign pathology. Thus, even after applying stringent mammographic criteria for malignancy, a large number of breast biopsies are unnecessary.

Because of these shortcomings, other imaging modalities such as ultrasound, Doppler flow velocity measurements, and magnetic resonance imaging (MRI) have been proposed as additional diagnostic tools for improving breast cancer detection. These techniques might increase the sensitivity but will likely further reduce the specificity for breast cancer detection [1].

Metabolic imaging techniques detect physiologic rather than structural changes associated with malignant tumors. These techniques such as positron emission tomography (PET) and single photon emission computed tomography (SPECT) have found widespread oncologic use because of their high sensitivity and specificity. Enhanced glucose metabolism of untreated malignant tumors was first reported by Warburg *et al.* in 1930. Whole-body PET with radiolabeled fluorodeoxyglucose (FDG), in particular, has been used to successfully detect a wide variety of cancer, including breast cancer [2]. However, existing commercial PET instruments are not optimal for imaging small breast cancers. PET instruments customized for breast applications have been shown to exhibit superior technical characteristics for imaging small lesions in breast phantoms [3].

Based on these facts, we tried to optimize a detector configuration for positron emission mammography (PEM) using a positioning algorithm based on neural networks and investigate the effect of crystal thickness on the spatial resolution and linearity of PET detectors.

1.1   Thesis Outline

The first chapter introduces the thesis and in the second chapter provides information about physical principles of PET imaging, PET instrumentation and positioning algorithms. The third chapter is an overview of current PEM designs. Monte Carlo simulations and neural networks are explained in forth and fifth chapters. The sixth chapter describes the methodology and the simulations done during the work. Our results are summarized in seventh chapter and finally in the eighth chapter our results are discussed and concluded, future work related to this thesis is also proposed.

2. THEORY

2.1   Historical Background of PET Imaging

Positron emission from radioactive nuclei was discovered in 1933 by Thibaud and Joliot. Then it was shown that, in general, two photons were emitted simultaneously after positron emission at almost 180º to each other. As soon after this as 1946 the potential importance in medicine of positron-emitting radionuclides produced in a cyclotron was suggested. This potential was based on the following properties of positron emitters [4]:

(i)   the radioactive species which decay by positron emission include ^{11}C, ^{13}N, ^{15}O and ^{18}F, all biologically important nuclides amenable to chemical substitution into organic molecules such as $[^{11}C]$-glucose, $[^{13}N]$-H_2O, $[^{15}O]$-CO_2 and pharmaceuticals;

(ii)   the technique lent itself to electronic collimation by dual photon coincidence counting. This offered a great sensitivity advantage over single photon counting techniques, which required physical (lead or tungsten) collimation;

(iii)   the short half-lives of many positron emitters helped to minimize radiation dose to the subject and allowed repeated measurements over a short duration. By contrast, most single photon emitters half-lives of hours to days.

The first clinical positron imaging device was used in 1952. The photograph of this scanner can be seen in Figure 2.1. Looking back to 1985, many PET scanners had been developed by that time, especially for studies of the brain [4]:

(i)   Scanditronix/University of Stockholm (PC 384-B): using 384 Bismuth germinate $Bi_4Ge_3O_{12}$ (BGO) crystals;

(ii)   The Cyclotron Company/MGH (TCC 4600): BGO and 480 crystals, which was also available in whole-body configurations;

(iii)   EG&G Ortec (NeuroECAT): using 264 BGO crystals;

(iv)   NIH (NeuroPet): 912 BGO crystals;

(v)   Nucletronix/Washington University (PETT IV): a time-of-flight PET system with 288 CsF crystals;

(vi)   AEL/Montreal (Therascan 3128): comprising 128 BGO crystals;

(vii)   Shimadzu/Akita (Headtome III): using 480 BGO crystals;

(viii) LETI Grenoble/Orsay: a time-of-flight PET system with 384 CsF crystals, also available as a whole body scanner.

Whole body scanners were also being developed such as [4]:

(i)   Scanditronix, which used a combination of BGO and gadolinium oxyorthosilicate Gd_2SiO_5 (GSO) to improve spatial resolution;

(ii)   Nucleonix/Washington University (SuperPETT): a time-of-flight CsF-based system;

(iii)   EG&G Ortec (ECAT III): BGO-based scanner;

(iv)   Berkeley Donner Lab: a high-resolution, single-ring device with 280 BGO crystals.
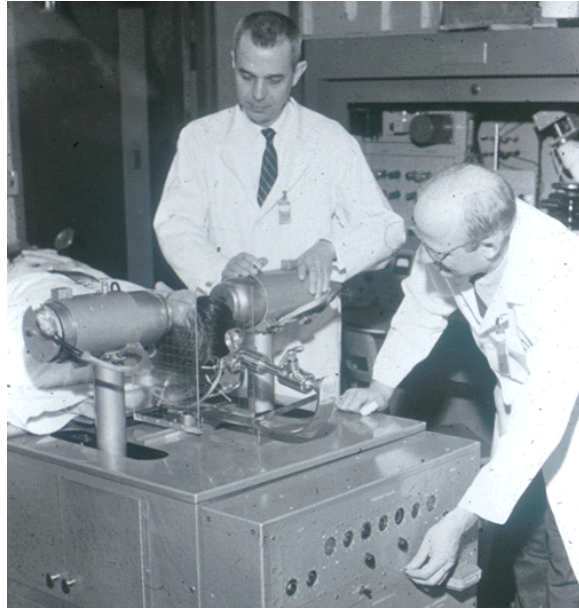
Figure 2.1 First positron imaging device [5].

Between the years of 1986 and 1991, new radiolabeled ligands and tracers are introduced and measurements of regional cerebral blood flow for activation studies are carried on. Due to the sensitivity restrictions, thought were given early on to operating the new block detector PET scanners in the "open" large-area camera mode. This involved removing the septa and recording all possible coincidences, thereby increasing the sensitivity. Due to the large radius of the detector rings and the use of deep shielding, much of the radioactivity from out of the field of view would be shielded from the detectors when the septa were removed. Full volumetric (3D) reconstruction came to the question [4].

From 1992 on, the block detector design was advanced by making both the block and the elements smaller. The former resulted in a reduction in scanner dead time through more parallel processing, and the latter in improved spatial resolution [4]. A comparison of several commercially available clinical PET systems is given in Table 2.1.

Table 2.1

Comparison of several clinical PET systems [6].

	ECAT EXACT 47	ECAT EXACT HR+	ECAT ACCEL	Advance NXi	C-PET plus	ALLEGRO
			Scanner			
Detector Material	BGO	BGO	LSO	BGO	NaI (Tl)	GSO
Diameter [cm]	82.4	82.4	82.4	92.7	90	90
Detector Dimensions [mm] (Transaxial × Axial × Depth)	$6.75 \times 6.75 \times 20$	$4.05 \times 4.39 \times 30$	$6.75 \times 6.75 \times 20$	$3.9 \times 8.2 \times 30$ mm	Curved Panel $500 \times 300 \times 25$ mm	$4 \times 6 \times 20$ mm
Detectors per Block or Module	64	64	64	36	1	638
Number of Rings	47	63	47	35	64/128	90
Axial FOV [cm]	16.2	15.5	16.2	15.2	18	25.6
Transverse FOV [cm]	58.5	58.5	58.5	55	57.6	57.6
Septa	Yes	Yes	No	Yes	No	No
Spatial Resolution [mm]						
2-D Transaxial:						
1 cm	6.0	4.6	6.2	4.8	—	—
10 cm	6.7	5.4	6.7	5.4	—	—
2-D Axial:						
1 cm	4.5	4.2	4.3	4.0	—	—
10 cm	5.9	5.0	5.9	5.4	—	—
3-D Transaxial:						
1 cm	6.0	4.6	6.3	4.0	5.0	4.8
10 cm	6.7	5.4	6.8	5.4	6.4	5.9
3-D Axial:						
1 cm	4.6	3.5	4.7	6.0	5.5	5.4
10 cm	6.5	5.3	7.1	6.3	5.9	6.5
Sensitivity [kcps/mCi/cc]						
2D	180	200	200	200	—	—
3D	780	900	925	1100	450	>700
Peak NEC [kCps]						
NEMA NU-2 (2001)						
2D	44	54	>90	83	—	—
3D	25	38	61	28	16	48

2.2 Physical Principles of PET Imaging

The nucleus of an atom is composed of nucleons, namely neutrons and protons. These nucleons have similar masses, but they differ in their charges, where proton has positive charge and neutron is uncharged. The nucleus is surrounded by electrons (e^-), which are negatively charged particles.

The nucleus is held together with strong force, which is an attractive force between nucleons and the Coulomb force, which is the repulsive force between positively charged protons. If a nucleus is unstable because of excess number of neutrons or protons, it is prone to radioactive decay, in order to achieve a more stable configuration. These types of nuclei are called radionuclides.

Radionuclides having an excess number of protons decay through positron (β^+) emission. The positron is the antiparticle of the electron, having the same mass but the opposite charge with the electron. During positron decay, a proton is converted into a neutron, a positron and a neutrino. An example of positron decay is shown in the Eq. 2.1.

$$^{11}\text{C} \rightarrow {}^{11}\text{B} + e^+ + \nu_e \tag{2.1}$$

In a positron decay, positrons are released with energies ranging between 0 and maximum energy E_{max}, where E_{max} is determined by the difference in atomic masses of the parent and the daughter atom. The emitted positrons have a mean kinetic energy of approximately 0.33 x E_{max}. Decay by positron emission is the basis for PET imaging.

Radioactive nuclei decay in an exponential fashion, where half-life is the time required for the half number of atoms to decay (Eq. 2.2). Radionuclides relevant for PET imaging and their half-lives are listed below, in Table 2.2.

$$A(t) = A(0)\exp(-\ln 2 \; x \, t/T_{1/2}) \tag{2.2}$$

where A(0) is the activity of the sample at time 0. Activity is measured in Becquerel (2.3) or in Curie (Ci) (2.4).

$$1 \text{ Bq} = 1 \text{ disintegration per second} \tag{2.3}$$
$$1 \text{ mCi} = 37 \text{ x } 10^6 \text{ Bq} \tag{2.4}$$

Table 2.2
Radionuclides for PET imaging [6].

Radionuclide	Half-life	E_{max}(Mev)	β^+ Branching Fraction
^{11}C	20.4 min	0.96	1.00
^{13}N	9.97 min	1.20	1.00
^{15}O	122 s	1.73	1.00
^{18}F	109.8 min	0.63	0.97
^{22}Na	2.60 y	0.55	0.90
^{62}Cu	9.74 min	2.93	0.97
^{64}Cu	12.7 h	0.65	0.29
^{68}Ga	67.6 min	1.89	0.89
^{76}Br	16.2 h	Various	0.56
^{82}Rb	1.27 min	2.60, 3.38	0.96
^{124}I	4.17 d	1.53, 2.14	0.23

The energy of emissions is given in units of electron volts (eV) and its conversion to Joule (J) is given below.

$$1 \text{ eV} = 1.6 \times 10^{-19} \text{ J} \tag{2.5}$$

2.2.1 Annihilation Phenomenon

When the positron is ejected following the positron decay, its energy is dissipated within 10^{-1} to 10^{-2} cm, depending on its energy, in inelastic interactions with atomic electrons in the tissue. When it is almost at rest, it combines with an electron and they form a state called "positronium", which lasts only about 10^{-10} seconds before "annihilation" occurs. The mass energies of the positron and the electron are converted into electromagnetic energy, when positron is assumed to be at rest. The energy released by this phenomenon can be computed from Einstein's mass-energy formula (Eq. 2.6).

$$E = mc^2 = m_e c^2 + m_p c^2 \tag{2.6}$$

where m_e is the mass of the electron (9.11×10^{-31} kg), m_p is the mass of the positron (9.11×10^{-31} kg) and c is the speed of light (3×10^8 m/s).

The energy is released in the form of high-energy photons, each one having energy of 511 keV, ensuring that energy and momentum is conserved. Assuming that the positron and the electron are at rest, when they annihilate, the two photons are emitted simultaneously in opposite directions (180° apart) (Figure 2.2).
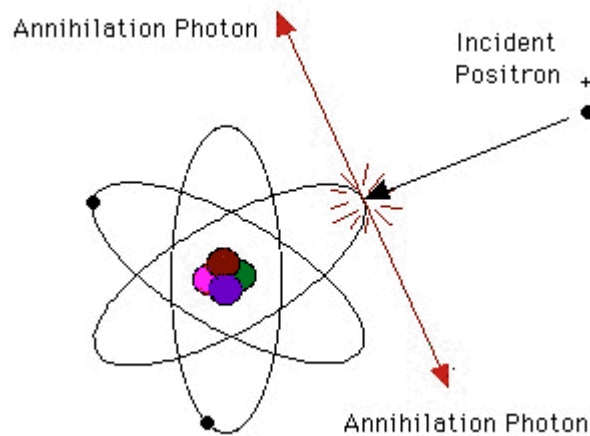
Figure 2.2 Annihilation phenomenon of an positron and an atomic electron [7].

If an annihilation occurs closer to detector 1, the photon directed towards detector 1 will reach the detector in a shorter time than the second photon directed towards the second detector. The relationship between this time difference and the location d, which is the hal-way between the two detectors, is given below (Eq. 2.7).

$$d = \frac{\Delta t \times c}{2}$$

(2.7)

This method is known as "time-of-flight", where it is very important to achieve a very good timing resolution, in order to be able to detect the coincidences by two opposite detectors.

2.2.2   Photon Interactions in Matter

Among a large number of possible interaction mechanisms for gamma rays in matter, there are three major types which play an important role in radiation measurements: photoelectric absorption, Compton scattering and pair production. In all these processes, the gamma-ray photon loses its energy partially or completely. It disappears completely or it is scattered through a significant angle.

2.2.2.1   Photoelectric absorption.   In photoelectric interaction process, a gamma photon undergoes an interaction with an absorber atom where it completely disappears. The photon loses its energy completely and an energetic photoelectron is ejected from one of the atomic shells of the absorber atom. For gamma-rays having enough energy, the most probable origin of the photoelectron is the K-shell of the atom. The energy of the ejected photoelectron is given below (Eq. 2.8).

$$E_e = h\nu - E_b \tag{2.8}$$

where E_b represents the binding energy of the photoelectron in its original shell and hν is the energy of the incoming gamma photon (Figure 2.3).

The vacancy left by the photoelectron can be filled with electrons from higher atomic shells of the atom. The binding energy between the two shells can be emitted as characteristic X-rays or the emission of an Auger electron may substitute for the characteristic X-ray.

The photoelectric absorption is the predominant interaction for gamma-rays of relatively low energy. The probability of photoelectric absorption also increases when the atomic number of the absorber increases. The probability is given by the Eq. 2.9.

$$\sigma_{photoelectric} \cong \frac{Z^n}{(E_\gamma)^{3.5}} \tag{2.9}$$

where n varies between 4 and 5 over the gamma-ray energy region of interest.
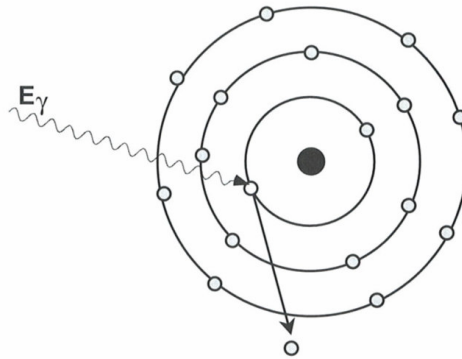
Figure 2.3 Representation of the photoelectric effect [4].

2.2.2.2   Compton scattering.   This type of interaction occurs between the incident gamma-ray and an electron of the absorber material. Compton scattering is the predominant interaction for gamma-ray energies of radioisotopes. In this type of interaction, the gamma-ray photon is deflected by angle θ with respect to its original direction. The photon transfers only a portion of its energy to an electron, called recoil electron. Because the photon can be scattered with different angles, the energy of the recoil electron can range between zero and a large fraction of the gamma-ray energy (Figure 2.4). The expression which relates the energy transfer and the scattering angle is given below.

$$hv' = \frac{hv}{1 + \frac{hv}{m_e c^2}(1 - \cos\theta)} \qquad (2.10)$$

where $m_e c^2$ is the rest mass of electron (511 keV), and c is the speed of light.

The probability of Compton scattering is linearly proportional to the atomic number of the absorbing atom.

The angular distribution of scattered gamma-rays is predicted by Klein-Nishina formula:

$$\frac{d\sigma}{d\Omega} = Z\,r_e^2 \left(\frac{1}{1+\alpha(1-\cos\theta)}\right)^2 \left(\frac{1+\cos^2\theta}{2}\right) \left(1+\frac{\alpha^2(1-\cos\theta)^2}{(1+\cos^2\theta)[1+\alpha(1-\cos\theta)]}\right) \quad (2.11)$$

where $\alpha \equiv h\nu/m_e c^2$ and r_e is the classical electron radius (2.82×10^{-15} m).
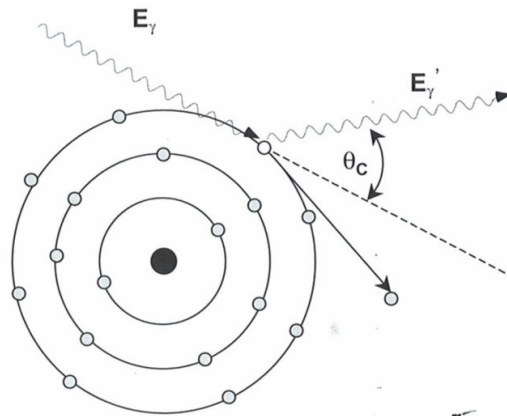
Figure 2.4 Representation of the Compton scattering [4].

2.2.2.3 Pair production.   Pair production is possible, when the energy of the photon is larger than twice the mass energy of an electron (1.02 MeV). In this type of interaction, the gamma photon disappears and an electron-positron pair is created, where charge and momentum is conserved (Figure 2.5). The difference of the energy of the photon and 1.02 MeV is required for the kinetic energy of electron-positron pair. The magnitude of the probability of pair production varies about the square of the atomic number of the absorber atom.
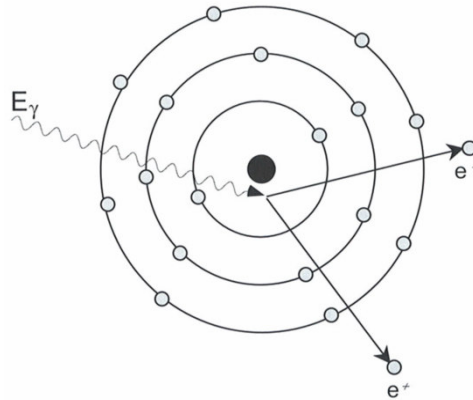
Figure 2.5 Representation of the pair production [4].

2.2.2.4 Attenuation. For a well-collimated source of photons, attenuation takes the form of a mono-exponential function:

$$I_x = I_0\, e^{-\mu x}$$
(2.12)

where I_x is the intensity measured through a material of thickness x, I_0 is the initial intensity and μ is the linear attenuation coefficient (units: cm^{-1}). Attenuation is dependent on the photon energy and the electron density of the attenuator. Each of the interaction processes removes the gamma-ray photon from the beam by absorption or by scattering and can be characterized by a probability of occurance per unit path length in the absorber. The linear attenuation coefficient is the sum of these probabilities (Eq. 2.13).

$$\mu = \tau(photoelectric) + \sigma(Compton) + \kappa(pair)$$
(2.13)

2.3   PET Instrumentation

A PET scanner consists of two or more detectors. Scintillation detectors are widely-used gamma-ray detectors for almost all PET scanners used today. These detectors are comprised of a dense crystalline scintillator material as an interacting medium for gamma-rays, which emits visible light. Then visible light is detected by a light photon detector and converted into an electrical current. The choice of scintillation crystals and visible light detectors is very important for getting a good performance indicated by the performance parameters for PET imaging.

2.3.1   Performance Parameters of PET

2.3.1.1   Spatial resolution.   The spatial resolution of a system represents its ability to distinguish between two points after image reconstruction. The measurement is performed by imaging point sources in air and then reconstructing images with no smoothing or apodization. The purpose of this measurement is to characterize the widths of the reconstructed image point spread functions (PSF) of compact radioactive sources. The width of the spread function is measured by its full width at half-maximum (FWHM) and full width at tenth-maximum (FWTM). The spatial resolution (FWHM and FWTM) of the point source response function in all three directions (radial, tangential, axial) is determined by forming one-dimensional response functions, along profiles through the image volume in three orthogonal directions, through the peak of the distribution [8].
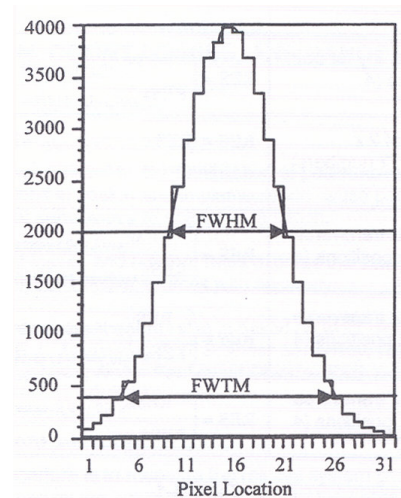
Figure 2.6 A typical response function with FWHM and FWTM determined graphically by interpolation [8].

2.3.1.2 Sensitivity.   Sensitivity of a positron emission tomography is expressed as the rate in counts per second that true coincidence events are detected for a given source strength. For the sensitivity measurement, a phantom filled with a certain amount of radioactivity and water is suspended in the center of the transaxial field of view, aligned with the axis of the tomography. This activity, A_{cal} in MBq, and the time of the assay T_{cal} are recorded. Data are collected for a period of time to ensure at least 10,000 true coincidences per slice are collected and then sensitivity is calculated. The sensitivity is calculated as indicated below.

$$S_{tot} = \frac{R_{CORR,0}}{A_{cal}}$$ (2.14)

where $R_{CORR,0}$ represents the count rate with no attenuation [8].

2.3.1.3 Energy resolution.   The detectors should be able to indicate the energy of the incoming annihilation photon such that those that have scattered in the body can be rejected. The ability of the detector to determine the energy of the photon is known as the energy resolution [1]. The energy resolution is conventionally defined as the FWHM divided by the location of the peak of the energy distribution (pulse height spectrum) [9].
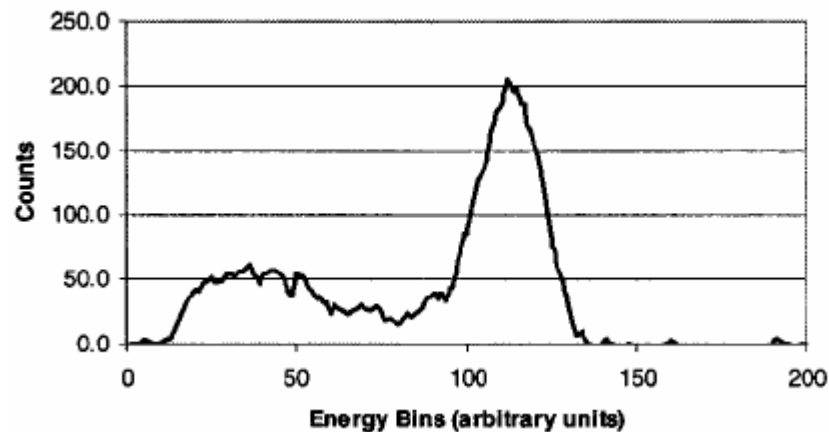
Figure 2.7 Pulse height spectrum [10].

2.3.1.4 Timing resolution.   It is defined as the ability of a pair of detectors to determine the time difference in arrival of annihilation photons and is typically on the order of 2 to 6 ns. A typical timing window that is used in PET scanners so as not accidentally reject annihilation photon pairs is typically 2 or 3 times the timing resolution, leading to values in the range of 4 to 18 ns [1]. The FWHM of the time distribution is used as the measure of the overall timing uncertainty in the measurement system [9].

2.3.1.5 Scatter fraction, count losses and random measurements.   The scattering of gamma-rays emitted by the annihilation of positrons results in falsely located coincidence events. Variations in design and implementation cause positron emission tomographs to have different sensitivities to scattered radiation. The measurements of count losses and random rates express the ability of a positron emission tomography to measure highly radioactive sources with accuracy [8].

2.3.1.6 Accuracy.   To achieve quantitative measurements of source activity distributionsunder widely varying conditions, positron emission tomographs usually have a capability to compensate for dead time losses and random events. The accuracy of these corrections, particularly at the highest count rates encountered in clinical imaging, is reflected by the bias with which the tomography reports counts [8].

2.3.1.7 Image quality, accuracy of attenuation and scatter corrections.   The purpose of this measurement is to produce images simulating those obtained in a total body imaging study with both hot and cold lesions. Spheres of different diameters are imaged in a simulated body phantom with non-uniform attenuation; activity is also present outside the scanner. Image contrast and signal-to-noise ratios (SNR) for both and cold spheres are used as measures of image quality. In addition, the accuracy of the attenuation and scatter corrections is determined from these measurements [8].

2.3.2   Scintillators

The scintillation process is one of the most useful methods for the detection of high-energy radiation. Scintillators have the property of emitting light in the visible region of the spectrum when high-energy photons deposit energy in them. The visible light is emitted isotropically and the amount of light emitted is proportional to the energy deposited. Scintillators can be organic or inorganic. For the purposes of PET imaging, dense, inorganic and solid scintillators are scintillators of choice. It is also clear that in the most dense scintillators, Compton interactions are more likely to occur than photoelectric interactions at 511 keV. Low-energy photons can be rejected by placing a lower threshold on the output. The surface treatment of the scintillator elements and the use of reflectors on the sides of the crystal are very critical. Stopping power and brightness of the scintillators are also important factors for scintillator choice, because integrated light signal from the scintillator is converted into electrons by the photodetectors and these signals are used for determining the location of the interaction. In both cases, the statistical fluctuations in the number of scintillation photons detected are a major source of noise in the measurements. These fluctuations have a characteristic of Poisson noise, where the standard deviation is $\sqrt{N}$ when the number of the detected photons is N. The decay time is another important factor in PET imaging because coincident detection of the two annihilation photons is involved. Finally, the index of refraction of the scintillator is also important as it determines how efficiently optical photons are transmitted from the scintillator to the photodetector. Table 2.3 gives the properties of scintillator materials used for gamma-ray detection at 511 keV in PET imaging [6,9].

Table 2.3
Properties of scintillators used in PET imaging [4].

Property	NaI(Tl)	BGO	LSO	YSO	GSO	BaF$_2$
Density (g/cm^3)	3.67	7.13	7.4	4.53	6.71	4.89
Effective Z	50.6	74.2	65.5	34.2	58.6	52.2
Attenuation length	2.88	1.05	1.16	2.58	1.43	2.2
Decay constant (ns)	230	300	40	70	60	0.6
Light output (photons/keV)	38	6	29	46	10	2
Relative light output	100%	15%	75%	118%	25%	5%
Wavelength λ(nm)	410	480	420	420	440	220
Intrinsic ΔE/E (%)	5.8	3.1	9.1	7.5	4.6	4.3
ΔE/E (%)	6.6	10.2	10	12.5	8.5	11.4
Index of refraction	1.85	2.15	1.82	1.8	1.91	1.56
Hygroscopic?	Yes	No	No	No	No	No
Rugged?	No	Yes	Yes	Yes	No	Yes
μ (cm^{-1})	0.3411	0.9496	0.8658	0.3875	0.6978	0.4545
μ/ρ(cm^2/gm)	0.0948	0.1332	0.117	0853	0.104	0.0929

2.3.3   Photosensors

High-energy annihilation photons are absorbed by the scintillator and the burst of low-energy optical photons that are emitted from the scintillator, are converted into an electrical current by the photodetectors. Each interaction produces a single electrical pulse. The pulse amplitude is determined by the number of visible light photons generated.

2.3.3.1   Photomultiplier tubes.   The majority of commercial PET scanners use photomultiplier tubes (PMTs). Visible light is transmitted through the glass entrance window of the PMT and the reaches the photocathode. Each light photon from the scintillator has about a chance of 15% to 25% to liberate an electron from the photocathode. This property is called the quantum efficiency of the PMT. Electrones are accelerated by a high potential difference towards the positively charged dynode and on the order of 3 or 4 secondary electrons are released, which are directed to the other dynodes, ultimately creating an avalanche of photoelectrons. PMTs have different sizes, shapes and models, like multichannel or position sensitive. The advantage of PMTs is their high gain, their stability, ruggedness and fast response. The disadvantages are that they are bulky and expensive.
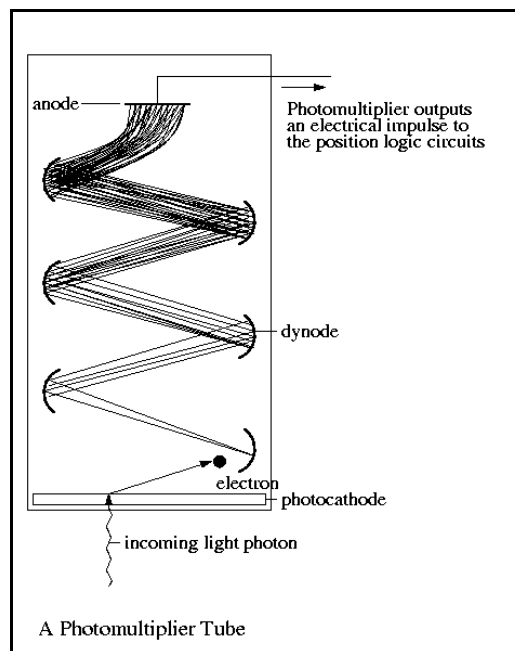
Figure 2.8 Cross-section of a PMT [11].

2.3.3.2 Solid state photodetectors.   Another photodetector used in PET imaging is the silicon photodiode (PD). A voltage of 10^2 or 10^3 V is applied across the silicon diode. When a scintillation light photon interacts in the silicon, it often has sufficient energy to liberate an electron from the lattice of the silicon. The vacancy it leaves behind is named as a hole and has a net positive charge. Under the applied electric field, the electron drifts toward the anode and the hole is drifted towards the cathode and an electrical signal can be measured. The quantum efficiency of photodiodes is around 60% to 80%, providing a much efficient conversion of photons to electrons compared to PMTs. But because they do not have an internal gain, the total signal measured is 10^6 times weaker than a PMT signal. This fact degrades the SNR and the ability to determine the energy deposited in the scintillator.

There is another type of photodiodes called avalanche photodiodes (APDs). Here, the voltage applied is much higher giving rise to an avalanche effect like in PMTs. Gains of 10^2 to 10^3 are possible providing a good SNR. Their quantum efficiency is like photodiodes, in the range of 60% to 80%. The energy and timing performance is roughly equivalent to those of PMTs (Figure 2.9).
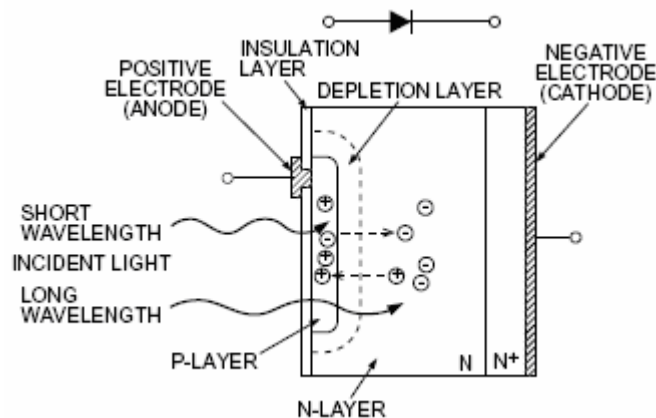
Figure 2.9 Cross-section of a PD [12].

2.3.4   Detector Configurations

2.3.4.1   Block detectors.   In this detector configuration, a relatively large block of scintillator material is segmented into an array of smaller detector elements. The saw cuts are filled with a white reflective material, in order to be able to isolate each element from the others. This detector block in Fig. 2.10 is coupled to four single-channel PMTs. The depth of the saw-cuts is determined so that the scintillation light is shared by the four PMTs in a linear fashion. Sufficient light produces a unique distribution of scintillation light in each detector element and so unique signals on the PMTs.

Figure 2.10 Block detector [13].

2.3.4.2   Quadrant-sharing detectors.   In this design, larger PMTs are used and each scintillation block is placed on the corner quadrants of four PMTs. Four PMTs are again being used to decode each block (Figure 2.11). The block in which the interaction occurs is determined by which four PMTs show a significant signal. One drawback of this approach is that it requires that blocks be structured into large planar panels and also there is not usable one half of a PMT width at each end of the panel.
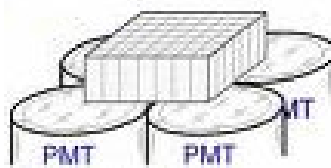
Figure 2.11 Schematic of the quadrant-sharing detector design [14].

2.3.4.3   Continuous detectors.   Other approach is to use large-area, continuous scintillator coupled to a matrix of PMTs (Figure 2.12). Thicker crystals are used for sufficient efficiency. For the detection of the location of interaction, signal from each PMT is digitized and weighted so that the position of the interaction is linearly dependent to the positions calculated from the PMT outputs. The position information provided is continuous, namely not like the discrete position information provided from block detectors. If the thickness of the crystal is increased to get a high SNR, a degradation of the spatial resolution is observed. Another drawback of this configuration is that edges of the scintillator plates yield poor spatial resolution, because the shape light distribution changes due to the interactions of the photons with the edges of the crystal.
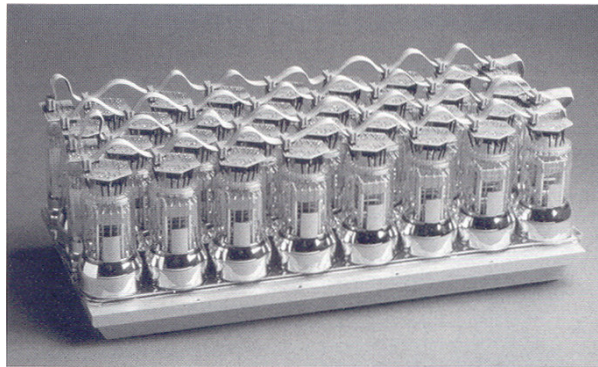
Figure 2.12 Photograph of large-area continuous scintillator coupled to a matrix of PMTs [6].

2.3.4.4   Detectors with PSPMTs or MCPMTs.   In several research PET systems single-channel PMTs have been replaced with multi-channel PMTs (PSPMT) and position sensitive PMTs (MCPMT) in various detectors. These are used for high-resolution PET systems because of their compact size and the ability to provide positional information. These devices are often used to decode arrays with large numbers of scintillator elements. The major drawbacks of PSPMTs and MCPMTs are the significant amount of dead space around their periphery and their high cost compared to single-channel PMTs.

2.3.4.5 Phoswich detectors.   The uncertainty in the depth of interaction (DOI) leads to degradation of spatial resolution in PET imaging. There are methods used to overcome this problem. The first approach is based on the use of two layers of scintillators with different

decay times, so that they can be differentiated. The layer in which the interaction is determined by looking at the decay times of the pulses. Another approach is to place the photodetectors (for example, a PIN photodiode and a single-channel PMT) at both ends of the scintillator and to use of the ratio of the signals of the photodetectors to get a measure of the DOI.

2.3.5   Limitations of PET Imaging

There are basically two effects in PET imaging causing errors in determining the line of response (LOR) along which a positron-emitting radionuclide is to be found. Blurring and limitation of spatial resolution are their major effects. Another limitation of PET is the detection of events other than true coincidences, like scatters or randoms as trues.

2.3.5.1 Positron range.   It is the distance from the site of positron emission to the site where the annihilation occurs. Positrons follow a turtous path because of the many direction-changing interactions before they annihilate with an electron. But the PET scanner detects the annihilation photons along the line passing through the site where the annihilation occurs and does not detect them along the path where the decaying atom is located. This effect causes a mispositioning and the blurring ranges from a few tenths of a millimeter up to several millimeters depending on the radionuclide and its E_{max}. Positron range limits also the ultimate resolution of PET.

2.3.5.2 Noncolinearity.   The cause of noncolinearity is the fact that positron and electron are not at rest when they annihilate. Because of that, the net momentum of these particles is not zero, so the angle between the two photons generated is not exactly 180º. The distribution of emitted angles is roughly Gaussian in shape with a FWHM of approximately 0.5º. The blurring effect coming from colinearity can be estimated as follows:

$$\Delta_{nc} = 0.0022 \times D \tag{2.15}$$

where D is the diameter of the PET scanner.

2.3.5.3 Detected events other than true coincidences.   Event detection in PET relies on electronic collimation. An event is regarded as valid if two photons are detected within a predefined elecronic time window known as coincidence window, the subsequent line-of response formed between them is within a valid acceptance angle of the tomograph and the energy deposited in the crystal by both photons is within the selected energy window.

But also unwanted events as one or both of the photons has been scattered or the coincidence is the result of the accidental detection of two photons from unrelated positron annihilations. The terminology commonly used to describe the various events in PET detection are (Figure 2.13):

(i)   A single event, which is a single photon counted by a detector. A PET scanner typically converts between 1% and 10% of single events into paired coincidence events;

(ii)   A true coincidence event, which is an event that derives from a single positron-electron annihilation. The two annihilation photons both reach detectors on opposing sides of the tomograph without interacting significantly with the surrounding atoms and are recorded within the coincidence timing window;

(iii)   A random coincidence occurs when two nuclei decay at approximately at the same time. After annihilation of both positrons, four photons are emitted. Two of three photons from different annihilations are counted within the timing window and are considered to have come from the same positron, while the other two are lost. Random events can be removed either by estimating the random event rate from measurements of the single event rates or employing a delayed coincidence timing window;

(iv)   Multiple events are similar to random events, except three events from two annihilations are detected within the coincidece timing window. Due to the

ambiguity in deciding which pair of events arises from the same annihilation, the event is disregarded. Again, multiple event detection rate is a function of count rate;

(v) Scattered events arise when one or both of the photons from a single positron annihilation detected within the selected coincidence timing window have undergone a Compton interaction. Compton scattering causes a loss in energy of the photon and change in direction of the photon. The consequence of counting a scattered event is that the line-of-response assigned to the event is uncorrelated with the origin of the annihilation event. This causes inconsistencies in the projection data, and leads to decreased contrast and inaccurate quantification in the final image.
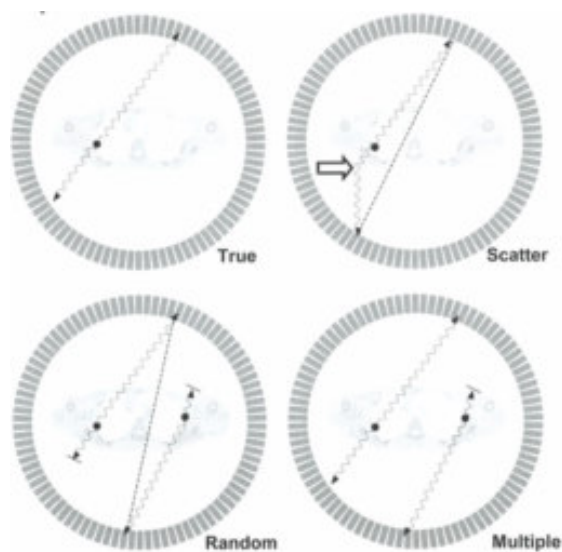
Figure 2.13 True, scatter, random and multiple events detected in PET imaging [4].

2.4   Photon Detection Algorithms

Physical restrictions of PET imaging limit the resolution and can hardly be improved, but with the improvement of detection algorithms for scintillation detection in

the crystal, the quality of PET scanners can be significantly improved. The quality of PET scanners is specified by several quantitative criteria explained in Section 2.3.

The geometric configuration of a PET detector has a significant effect on the spatial resolution. If the scintillation point is far from the photodetector, the solid angle subtended by the photodetector and inevitably the number of photoelectrons produced, decreases. As a result, a higher uncertainty is observed in the received signal and the position estimation worsens. These distant events are much more subjected to edge effects, like multiple reflections and refractions. In such regions, the distorted light distribution causes the spatial resolution to degrade.

Another important problem in scintillation detection is the parallax effect (Figure 2.13). If the crystal thickness is increased, in order to prevent the escapes and in that way to improve the sensitivity of the scanner, non-normal photons cause parallax effect, which depends on the depth of penetration of the gamma-ray and the sine of its incidence angle.

$$\delta_{p} = \Delta z \cdot \sin \theta \tag{2.16}$$
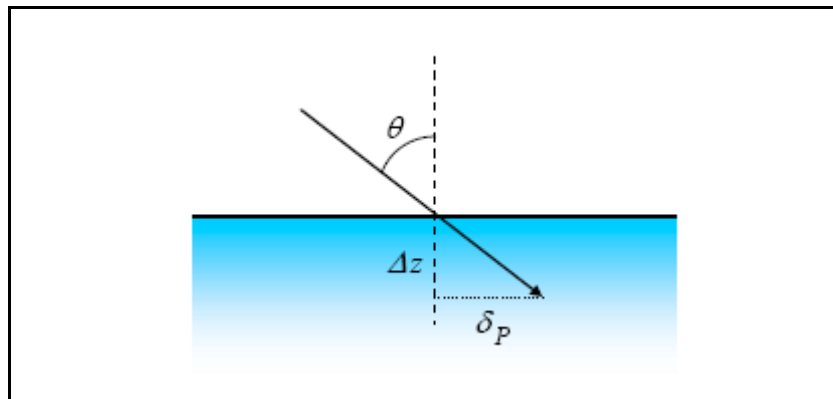
Figure 2.14 Parallax effect in a thick scintillation crystal [15].

To overcome these problems and to obtain good performance characteristics, many positioning algorithms are developed.

2.4.1 Anger Algorithm

Anger algorithm is commonly used for scintillation positioning in nuclear medicine imaging. It is a centroid-based algorithm and calculates the scintillation coordinates with fixed weights given to photodetectors with respect to a certain point in the crystal, which is generally the center point.

$$x_{est} = \sum_i \omega_i(x) V_i , \tag{2.17}$$

$$y_{est} = \sum_i \omega_i(y) V_i \tag{2.18}$$

where $\omega_i(x)$ and $\omega_i(y)$ are the weights of the ith PMT in x and y directions with respect to the center of the crystal, respectively.

An improvement to Anger algorithm is done with threshold pre-amplification for each PMT. Based on the fact that distant events cause more uncertainty than the near ones, less strong weights are assigned to the distant PMTs with threshold amplification of signals, such that larger output signals receive greater amplification than weaker ones.

A second improvement to this algorithm is the bias correction. Bias is observed mostly for the regions distant from the center and it is tried to be overcome by subtracting an estimated bias value from the calculated coordinates according to the region estimated by the uncorrected Anger algorithm.

A third approach is placing virtual PMTs at the crystal edges and assigning realistic signal values to them on a event by event basis on the signals of nearby lying real PMTs. This approach is proposed in order to eliminate the degradation of spatial resolution at the edges [16].

2.4.2 Statistical and Look-Up-Table (LUT) Based Algorithms

As a result of the bias problem of Anger algorithm, bias-free positioning algorithms are being investigated. One of these methods is the use of maximum-likelihood (ML) algorithm. ML based techniques have been developed in order to achieve efficient position estimators. It has been reported that ML algorithm offers advantages of improved spatial resolution and bias over conventional Anger algorithm and the useful field of view (UFOV) of the detectors is increased by using this algorithm. The basic principle of the ML method is to select the scintillation positions which maximize the probability of obtaining such PMT responses for a set of observed PMT responses. Line-response-functions (LRF) are determined experimentally by moving a point or line source on a known grid with a certain precision and observing each PMT response according to the source position. Later studies have improved this algorithm by adding also the DOI information and interpolating the PMT responses or fitting them in Gaussian or Poisson curves, eliminating the discontinuities or calculating them according to the solid angle coverage instead of measuring them with a lot of time consumption [17-21].

Other algorithms are developed which involve generation of crystal LUTs for PMT responses or flood histograms. These are implemented for pixellated and continuous crystals mounted on position sensitive APDs (PSAPD) and PMTs, respectively. These involve the use of nearest neighbor position estimation or other algorithms for estimation of detector intrinsic resolution and DOI. It is reported that the DOI affects the location estimation and therefore the resolution and the resolution is improved by using the LUT based positioning algorithm [22,23].

2.4.3 Neural Network Based Algorithms

Another group of algorithms for accurate position estimation uses artificial neural networks (ANN) where the capability of the ANNs for modeling the detector response is used. The thought behind is to develop scanners with lower costs using continuous thick crystals to increase the sensitivity without sacrificing the spatial resolution. It is shown that implementation of ANNs enables fast, bias-corrected position estimation and correction of

non-linearities making the real time line-of-response (LOR) computation possible. It is also found out that incorporation of information about angles improves the accuracy of the position estimation [24,25].

3. CURRENT PEM DESIGNS

Development of special purpose, dedicated PET scanners is an important issue in PET research. This fact is also valid for breast imaging. Many research groups have been developing so called PEM cameras since 1990's. The need of use PEM arises from the fact that these scanners restrict the field of view (FOV) to a single breast, cover a larger solid angle around the breast, have higher efficiency and have lower cost compared to conventional PET scanners for detecting breast cancer.

The most common geometry consists of two planar detector modules, but there are other researchers who investigated PEM tomographs, cylindrical, hexagonal, rectangular or curved plate PEM configurations.

The first breast dedicated scanner is begun to be constructed by Thompson *et al.* [27] after a feasibility study done in 1994, where Monte Carlo (MC) simulations of a breast phantom made using PETSIM are compared with actual scans of this phantom in a conventional whole-body PET scanner [26] (Figure 3.1). Their configuration consists of two planar BGO blocks of dimensions 36 x 36 x 20 mm cut into 2 x 2 mm squares coupled to two 7.5 cm square PSPMTs (Hamamatsu R3941-05) and coincident events are back-projected to form real-time multiple plane images. The sensitivity of the camera is about 20-fold of the sensitivity of a conventional PET scanner achieving a reduced patient dose and cost per scan. The device is expected to have an in-plane spatial resolution about 2 mm full-width-at-half-maximum (FWHM)**.**
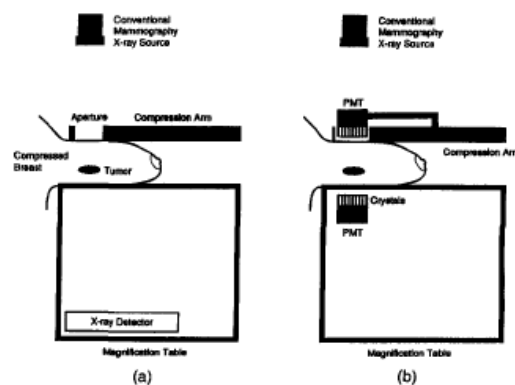
Figure 3.1 Schematic of the proposed positron emission mammography device. **(a)** X-ray detector with compression member, **(b)** X-ray detector and the integrated PEM camera [26].

In 1996 [28], the spatial resolution in the central region is measured to be 2.05 mm FWHM when only near normal LORs are accepted, this measured value was less than half that of a conventional whole-body PET scanner. In the case of accepting of all LORs, the spatial resolution is found to be 2.75 mm by the researchers. That year the effects of cutting, etching and potting on the spatial resolution are also investigated, and the spatial resolution is found to be of 3.22 mm, 2.61 mm and 2.05 mm FWHM, respectively. Thompson *et al.* [29] acquired the early clinical results from PEM-1 after scanning 11 patients in the year of 1998. 2 false-negative results, 5 true-positives, 4 true-negatives and no false-positives are observed and based on these results the system sensitivity is estimated at 71%, the specificity at 100% and the accuracy at 82%. In 2000, the timing resolution is calculated to be 12 nsec and besides the effect of increasing the low energy threshold is studied and it is seen that scattered events are decreased, resulting in improved image contrast at the cost of the system efficiency (Figure 3.2).
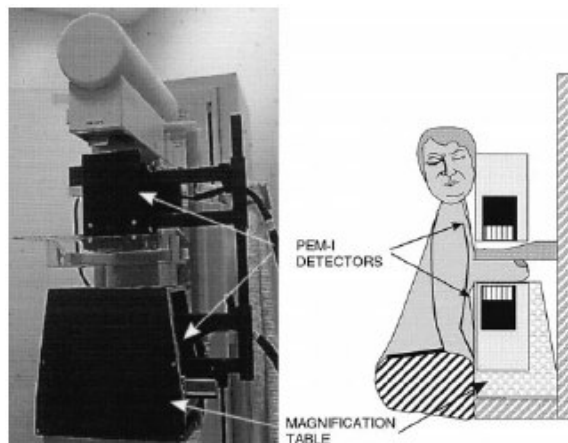
Figure 3.2 PEM-1 and the detailed patient position during scanning [29].

Further investigations [30] showed that the completed system has a spatial resolution of 2.8 mm FWHM and new clinical PEM results are compared with X-ray mammography results (Table 3.1).

Table 3.1
Comparison of PEM and mammography results by Murthy *et al.* [30].

Index	Method of calculation	Imaging modality (%)	
		PEM	Mammography
Sensitivity	TP/(TP + FN)	80	90
Specificity	TN/(FP + TN)	100	50
Accuracy	TP + TN/(TP + TN + FP + FN)	86	78
Positive predictive value	TP/(TP + FP)	100	81
Negative predictive value	TN/(TN + FN)	67	67

TP = true-positive; FP = false-positive; FN = false-negative; TN = true-negative.

In the year of 1995, Moses *et al.* [31] presented another design of PET camera dedicated to breast imaging with high sensitivity and specificity, but low cost and injected FDG-dose. This design extends a previous design (Thompson *et al.* 1994) by completing the detector ring around the breast and constructing the detector ring with modules with DOI measurement resolution. The detector module consists of an 8 x 8 array of 3 mm x 3 mm x 25 mm lutetium oxyorthosilicate Lu_2SiO_5:Ce (LSO) crystals coupled on one end to a PMT and on the other end to a silicon photodiode (PD) array. With these improvements, sensitivity is increased, angular sampling is improved and the extreme parallax errors are reduced. This geometry is calculated to have 100-fold greater sensitivity, 4-5-fold increased solid angle and a 20-fold lower attenuation than a conventional whole-body PET camera. In 1998, a 2D Fourier-based reconstruction algorithm is presented by the same group (Virador *et al.* 1998 [32]) and spatial resolution is calculated via simulation studies and also with the realistic camera. The camera is composed of 14 modules, each an 8 x 8 array of 3mm x 3 mm x 30 mm crystals (Figure 3.3), mounted on a PMT for timing and a PD array for crystal interaction identification. The patient port is 9.6 cm x 6.0 cm.
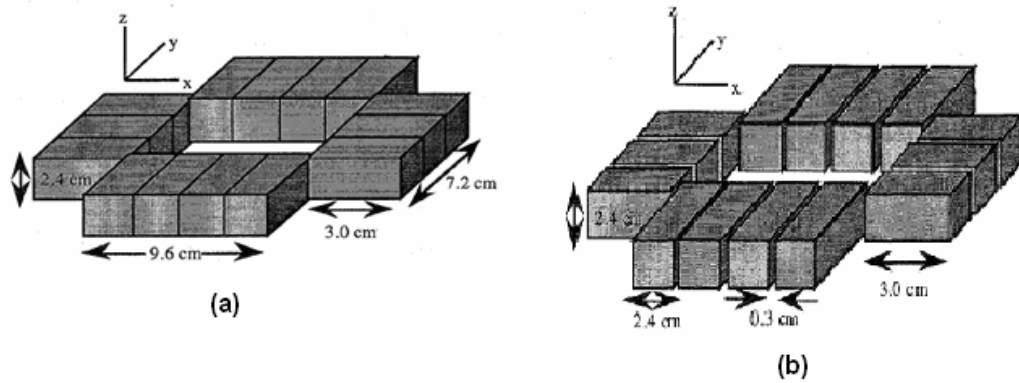
Figure 3.3 PET camera design for imaging breast cancer and axillary node of Virador *et al.* **(a)** Simplified geometry showing modules, **(b)** Realistic camera geometry [32].

The spatial resolution of the camera is found to vary between 1.9 mm 2.8 mm FWHM, depending on the position of the point source in the FOV (Table 3.2) [32].

Table 3.2

Spatial resolutions found by Virador et al. **(a)** Spatial resolution at various locations in the simplified detector for various DOI, **(b)** Spatial resolution at various locations in the realistic camera [32].

PSF Resolution for Various DOI Resolution			
Location	0 mm	5 mm	10 mm
(0.0, 0.0)	1.74(0.06)	1.90(0.05)	1.90(0.08)
(1.0, 0.0)	1.73(0.04)	2.15(0.13)	2.51(0.28)
(0.0, 1.0)	1.74(0.05)	2.17(0.04)	2.52(0.22)
(2.5, 1.5)	2.03(0.15)	2.35(0.06)	2.67(0.10)
(4.6, 0.0)	1.85(0.45)	2.81(0.12)	2.70(0.33)
(0.0, 2.8)	1.83(0.46)	2.70(0.08)	2.50(0.09)
(4.6, 2.8)	2.05(0.35)	2.51(0.14)	2.50(0.15)

(a)

Location	PSF FWHM
(0.0, 0.0)	1.92(0.16) mm
(1.0, 0.0)	2.14(0.13) mm
(0.0, 1.0)	2.37(0.13) mm
(1.5, 2.5)	2.42(0.10) mm
(4.6, 0.0)	2.81(0.21) mm
(0.0, 2.8)	2.44(0.22) mm
(4.6, 2.8)	2.79(0.23) mm

(b)

In the year of 2001, Virador *et al.* [33] presented 3D reconstruction algorithms with irregular sampling and DOI for a camera dedicated to breast and axillary node imaging. Each detector module of the camera consists of 64 detector elements, each 3 mm x 3 mm x 30 mm. As a result of MC simulations, artifact free and spatially isotropic images are obtained and spatial resolution is calculated to be 1.5 mm, 2.3 mm and 3.1 mm, at the

center, in the bulk and in the corners of the FOV, respectively. The results are summarized in Table 3.3.

Table 3.3
FWHM of point sources in various locations of the FOV by Virador et al. [33].

(X,Y) Location (cm)	PSF FWHM (FOV Center)	PSF FWHM (FOV Edge)
(0.0, 0.0)	1.54 mm	1.91 mm
(5.4, 0.0)	2.50 mm	2.60 mm
(2.7, 1.6)	2.14 mm	2.45 mm
(0.0, 3.2)	2.63 mm	3.10 mm
(5.4, 3.2)	3.10 mm	3.18 mm

In 1996, Weinberg et al. [34] proposed another PEM device which is mounted in a conventional X-ray mammography gantry. Each planar gamma-ray detector consisted of a slab of 1 cm thick BGO crystal coupled to a position-sensitive photomultiplier (Hamamatsu R3941 PS-PMT). The FOV is 6 cm by 6 cm. The spatial resolution is 3.1 mm FWHM and it is concluded that it is possible to image a breast cancer with a dedicated PEM scanner, mounted in a conventional mammography unit in less than 5 min with minimal breast compression (Figure 3.4).
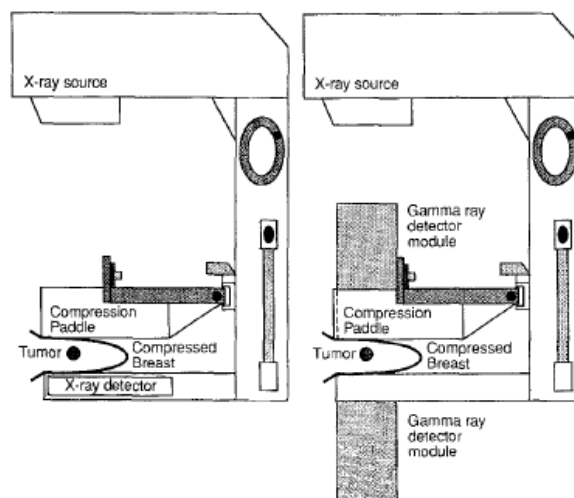
Figure 3.4 Geometry for PEM of Weinberg *et al.*[34].

In the year of 2002, Weinberg *et al.* [35] constructed a PEM scanner where two detector heads able to move under computer control fit within custom paddles. The purpose of this travel is to bring in flexibility in order to acquire a full-breast image or to sweep the detector heads across the central portion of the breast. Each of the two PET detector heads consists of 12 arrays of 13 x 13 lutetium-based crystals where each crystal was of size 2mm x 2 mm x 10 mm. The spatial resolution of the system is measured to be 2.6 mm FWHM using a Na-22 source (Figure 3.5).
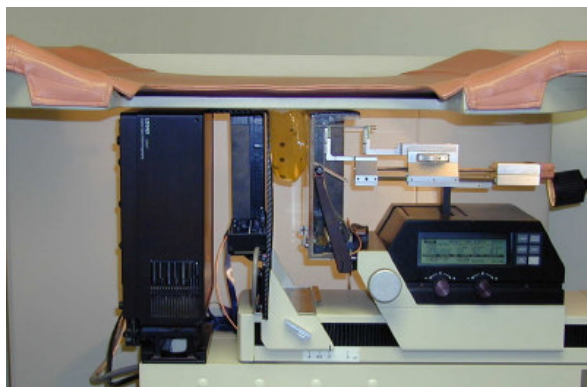
Figure 3.5 PEM-2400 detector [35].

In 1997, Freifelder and Karp [36] asserted that thalium doped sodium iodide (NaI(Tl)) detectors can be adapted for a breast imaging scanner and use of small detectors to optimize spatial resolution and sensitivity. To separate the breast from the body, in order to make the breast more uniform and less variable in density, it is proposed that the patient lies in a prone position and letting her breast hanging away from the chest wall. So attenuation correction may not be necessary. Two designs have been considered, one is a small ring of NaI(Tl) to surround the breast and the other configuration uses two flat detectors placed on the opposite sides of the breast. The ring geometry is thought to preclude imaging of the lymph nodes and the axillary tail, but the planar geometry can provide a more flexible geometry and allows imaging of breasts of different sizes. However, it also has limitations like lack of complete angular sampling. Both configurations are simulated. For the ring configuration, the separation distance between the detectors is set to 17.2 cm to accommodate different breast sizes. The detectors are simulated to be 20 cm long and 9 or 19 mm thick and the detector resolution is found to be

4.0 mm and 4.7 mm, respectively. Stationary planar detectors are also investigated, two 20 cm x 20 cm detectors with either 9 mm or 19 mm thicknesses are simulated. The separation between the detectors are set to be 10 cm and detector resolution is again found to be 4.0 mm and 4.7 mm, respectively (Figure 3.6).
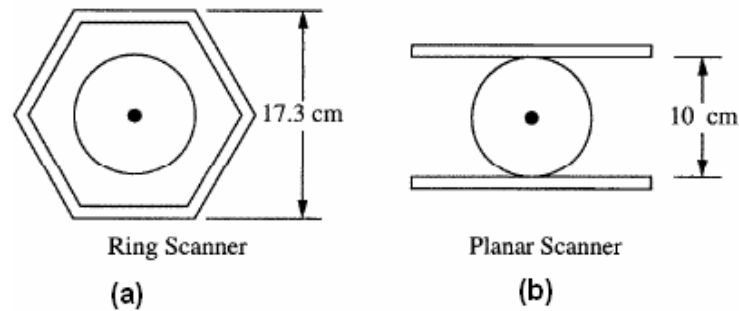
Figure 3.6 Dedicated PET scanner of Freifelder *et al.* **(a)** Ring scanner configuration, **(b)** Planar scanner configuration [36].

In the year of 2002, Freifelder *et al.* [37] presented the first imaging results from phantom measurements of a dedicated, breast-only positron emission imager, BPET, which uses 19 mm thick curve plate NaI(Tl) detectors in a split-ring design. The detectors surround the breast of the patient when the woman lies prone letting her breasts hang down from the body (Figure 3.7). Each detector is instrumented with forty-five 39 mm diameter PMTs and the active area of each is 22 mm from the top surface of the detector and the total active area is 28 cm x 21 cm. The detectors are mounted on a flexible gantry whose separation can be varied from 10.6 cm to 60 cm (Figure 3.8). The measured energy resolution of the system is 10% at 511 keV. The radial spatial resolution is 3.8 mm at r = 0 cm and 4.5 mm at r = 5 cm.
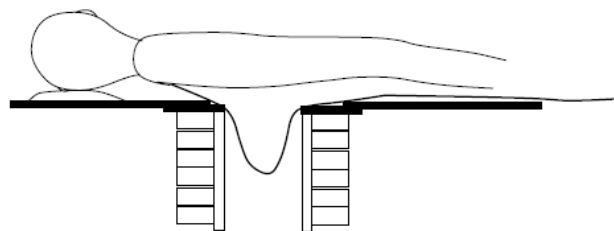
Figure 3.7 Schematic diagram of BPET showing the woman lying prone [37].
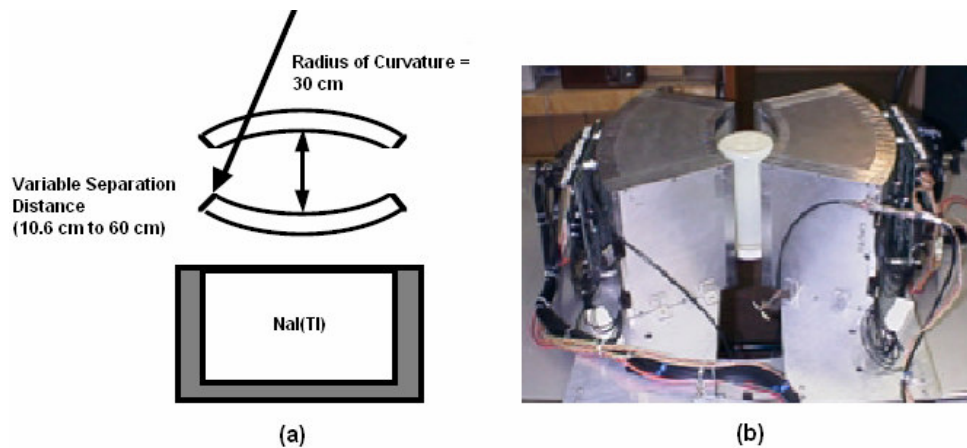
Figure 3.8 BPET breast imager **(a)** Schematic of the curve plate detectors and the housing of the NaI(Tl) crystal, **(b)** Completed prototype of BPET breast imager [37].

Raylman *et al.* [38] carried out a phantom study to investigate the capabilities and limitations of PEM in detecting breast tumors in 2000. Initially, basic scanner parameters like resolution, sensitivity and scatter fraction are measured and the effect of breast imaging parameters like length of acquisition, breast thickness and breast density are also explored utilizing phantoms. The PEM imager consists of two opposing detectors. Each detector contains a 4 x 4 array of compact Hamamatsu R5900-C8 PSPMTs and a 30 x 30 array of GSO crystals which has a higher light output and shorter pulse widths. Each GSO crystal has dimensions of 3.1 mm x 3.1 mm x 10 mm. The completed PEM scanner has a square FOV of 10 cm x 10 cm and the average pixel spacing was 3.3 mm. An energy discrimination window of 400-600 keV is applied to the data in order to reduce acceptance of Compton scatters and a confocal reconstruction algorithm is used to produce planar images. The FWHM of the line spread functions (LSF) are calculated to be between a range of 3.9 mm and 4.6 mm, at the center of the FOV and at distances of ± 3 cm from the center of the imager. In thin compressed breasts (2 cm) spheres of 5 mm diameter can be detected, where increased breast thickness increases the minimum detectable sphere size to 8 mm.

An initial experimental evaluation of 3D breast imaging with tomographic acquisitions using dual planar detectors is made by Smith *et al.* [39] in the year of 2004 and compressed breast phantom and point source studies are compared with the stationary PEM. The breast scanner used is the design of Raylman et al. (2000) [38], using R7600-C8

PSPMTs, instead of R5900-C8 (Figure 3.9). Two tomographic datasets are created with rotational increments of 20º and 60º. Point sorce studies show that for stationary PEM averaged resolution is 0.89 ± 0.18 cm FWHM normal to the detector and 0.37 ± 0.07 cm parallel to it when all LORs are included. For tomographic acquisition of 60º increments, the averaged radial resolution is 0.55 ± 0.06 cm and the averaged tangential resolution is 0.9 ± 0.08 cm at 4 cm from the axis of rotation (AOR). The radial resolution for the 20º increment data is 0.57 ± 0.03 cm and the tangential resolution is 0.9 ± 0.03 cm again 4 cm from AOR. Reconstructions of the compressed breast phantom showed excellent lesion visualization for all PEM and PEM tomography (PEMT) acquisitions (Figure 3.10).

(a)   **(b)**
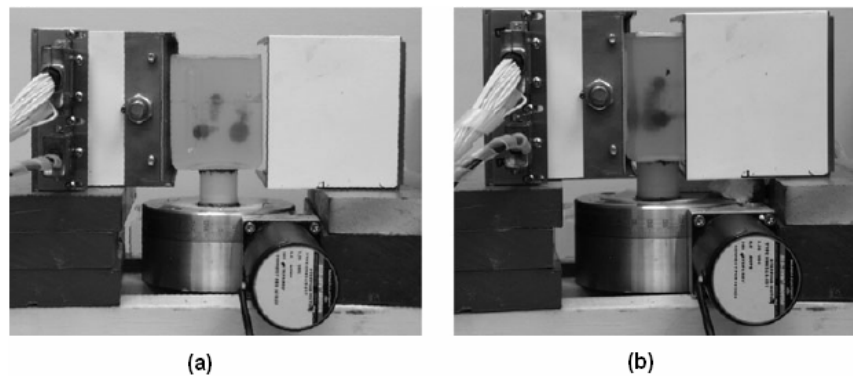
Figure 3.9 PEM design by Smith *et al.* **(a)** Side view of the detectors with a separation of 10 cm for tomographic acquisitions and the compressed breast phantom at a 90º rotation angle, **(b)** Compressed breast phantom at a zero degree rotation angle with a detector separation of 6.3 cm for one of the static PEM acquisitions [39].

(a)   **(b)**   **(c)**
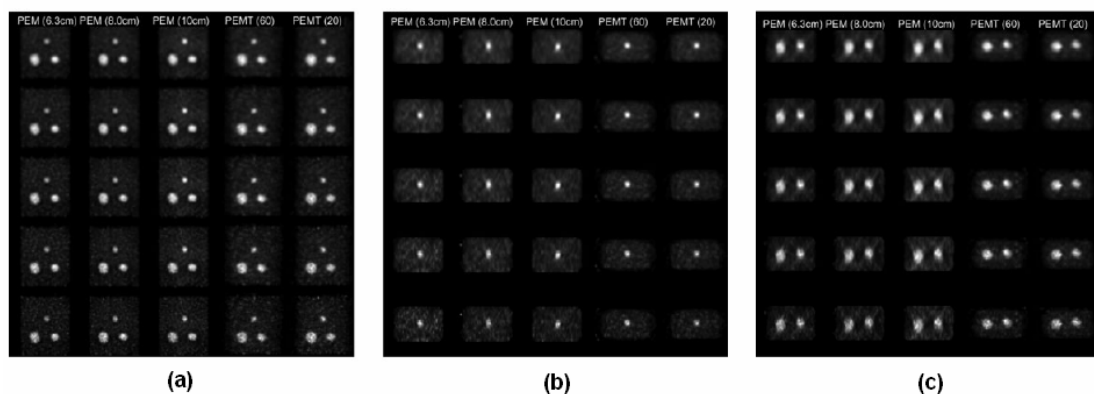
Figure 3.10 Slices through image reconstructions of the compressed breast phantom, **(a)** perpendicular to compression direction (parallel to detectors for the single angle PEM case), **(b)** normal to the detectors .through the 9 mm sphere (normal to the axis of rotation (AOR) for PEM tomography) and **(c)** normal to the detectors through the 12 and 15 mm spheres (and normal to the AOR for PEM tomography). From left to right the columns are (1) PEM, 6.3 cm detector separation, (2) PEM, 8.0 cm detector separation, (3) PEM, 10.0 cm detector separation, (4) PEMT, 10 cm detector separation and 60º rotation increment and (5) PEMT, 10 cm detector separation and 20º rotation increment. The rows from top to bottom are with 4.0, 3.5, 3.0, 2.5 and 2.0 mm FWHM 3D post-reconstruction Gaussian filters. Each subimage slice is scaled to its own maximum [39].

Doshi *et al.* [10] designed and developed a modular PET detector that is composed of a 9 x 9 array of 3 mm x 3 mm x 20 mm LSO scintillator crystals couple to an optical fiber taper, which is coupled to a Hamamatsu R5900-C8 PSPMT, which has a surface area of 3 cm x 3 cm and an active photocathode area of 2.2 cm x 2.2 cm (Figure 3.11). Irradiating the detectors with radioactive isotopes, the average energy resolution for the entire detector module is found to be 19.5% with a standard deviation of 1.3%. The timing resolution of the system is 2.4 ns and according to the point spread function of the entire row of crystals, the spatial resolution is measured to be 2.3 mm, with the worst being 2.6 mm. The energy threshold applied is chosen to be 350 keV.
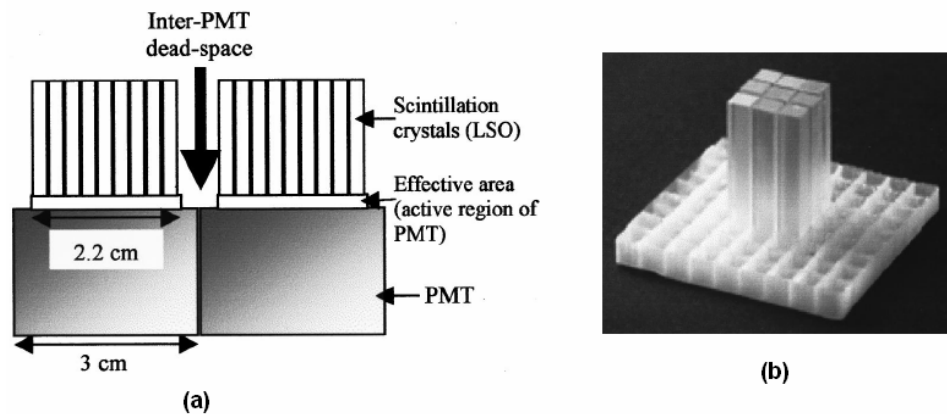
Figure 3.11 PET detector design by Doshi *et al.* **(a)** Coupling of scintillator arrays to Hamamatsu R5900-C8 PSPMTs, **(b)** A picture of plastic grid showing 9 of 81 LSO crystals in place. The wall thickness is 0.3 mm [10].

In 2001, Doshi *et al.* [40] improved their previous design and presented a new breast scanner mammary and axillary region PET (MaxPET). The system consists of two planar detector plates of size 15 cm x 15 cm, each of which is composed of 5 x 5 modular detectors. The modular detectors are each composed of a 9 x 9 array of 3 mm x 3 mm x 20 mm LSO scintillator crystals couple to an optical fiber bundle, which is coupled to a Hamamatsu R5900-C8 PSPMT. The optical fiber bundle is composed of many thousands of micron diameter glass fibers used together (Figure 3.12). An acrylic phantom is filled with FDG and imaged. The averaged energy resolution for detector plate 1 is 22.9% and for detector plate 2 is 20.4%. The time resolution is measured to be 8.1 ns FWHM. The

resolution in projection images is 4 mm based on profiles taken through the line source phantom images.
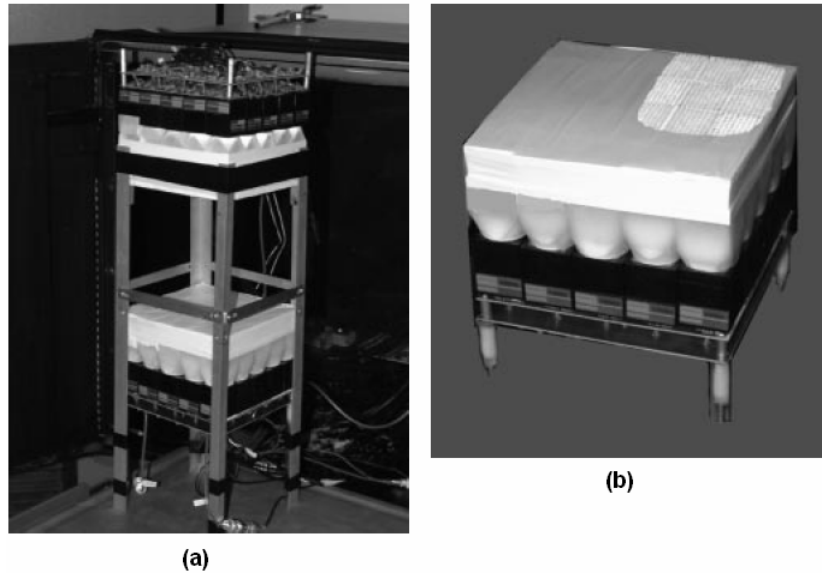
Figure 3.12 MaxPET detector design **(a)** A picture of MaxPET assembly, **(b)** A Maxpet detector plate [40].

Lecoq and Varela [41] proposed in 2002 the Clear-PEM concept. The basic component of the proposed system is lutetium aluminum perovskite Lu_2AlO_3 (LuAP) crystal developed by Crystal Clear Collaboration at CERN. LuAP has a density of 8.34 g/cm^3. (LSO and BGO have densities of 7.4 g/cm^3 and 7.1 g/cm^3, respectively.) Its light yield is about 10 photons/keV. (Light yield of LSO is 27/keV and of BGO is 9 photons/keV.) The emission spectrum has its peak at 365 nm and the time constant is 18 ns (compared to 40 ns for LSO and 300 ns for BGO). The energy resolution of LuAP is approximately 10% FWHM. The crystal dimensions are thought to be 2 mm x 2 mm x 20 mm according to its properties. The detectors are based on two planar plates, each formed 8 x 4 crystal matrices. The total number of crystals is 3000 and the surface area of each plate is about 10 cm x 12 cm. The planes are thought to be able to rotate to collect data in several orientations for 3D iamge reconstruction. The "phoswich" technique (LuAP and LSO) is thought to be used in order to obtain DOI information. APDs are planned to be used instead of PMTs or PSPMTs because of its advantages explained in Chapter 2.

In 2004, Ribeiro *et al.* [42] presented a simulation study of Clear-PEM with the dimensions explained in detail above [41]. Simulations are done using a dedicated MC simulation platform GEANT4 and ROOT. Three additional modules are developed, which are *PhantomFactory* to simulate radioactive decay in different phantoms, PEMsim to perform the detector simulation and DIGITsim to simulate the signal formation process in the scintillation crystals, photosensors and associated electronics. The intrinsic resolution of Clear-PEM for a point source in the center of the FOV is estimated to be 1.2 mm FWHM. DOI studies are made for a single LuAP:Ce crystal with double side readout and with the best configuration, DOI resolution is found to be 2.4 mm FWHM. Abreu *et al.* made another study to evaluate the performance of the imaging system Clear-PEM in the year of 2006. The camera consists of detector heads having dimensions of 16.5 cm x 14.5 cm for breast and axilla imaging. The design is renewed to have cerium doped lutetium yttrium orthosilicate $Lu_{2(1-x-y)}Y_{2x}SiO_5:Ce_y$ (LYSO:Ce) crystals of dimensions 2 mm x 2 mm x 20 mm and with different surface treatments, polished, slightly polished and rough. All crystals are coupled to Hamamatsu S8550 APD matrices. The energy resolution is observed to be 13% FWHM at 511 keV with flood irradiation. Performing phantom measurements, after 10 Expectation Maximization (EM) iterations, the point source in the center of the FOV presents a transaxial and axial spatial resolution of 1.4 mm FWHM. If the point source is placed 2.5 cm away from the center of the FOV, transaxial and axial resolutions are measured to be 1.7 mm and 2.6 mm, respectively [43].

In 2003, Adler *et al.* [44] introduced another PEM device mounted on a streotactic X-ray mammography unit, in order to demonstrate the feasibility of a hybrid functional/anatomic breast imaging platform with biopsy capability for facilitating lesion detection and diagnosis. Their design differs from first versions in the choice of detector crystal. They use pixellated GSO crystals of 3 mm x 3 mm x 15 mm having a short time of 30 nsec, enabling better handling of high count rates and permitting reduced shielding requirements. The effective FOV is approximately 5 cm x 5 cm. The spatial resolution is measured with point sources as approximately 2.5 mm FWHM (Figure 3.13) and in 2003 Levine *et al.* [45] accomplished a study in women scheduled for stereotactic breast biopsy using the design of Adler *et al.* [44]. 18 breast lesions are evaluated, among which 7 were carcinoma and 11 were benign. The lesion-to-background ratio is found between a range of

1.32 and 7.7, where the average ratio for malignant lesions was 3.95 and for the benign ones was 1.94. The findings are listed in Table 3.4.

Figure 3.13 Geometry for PEM detector by Adler et al. After PEM image acquisition, X-ray-guided biopsy can proceed without releasing breast compression [44].

Table 3.4
Clinical findings of Levine *et al.* [45].

Patient no.	Pathologic diagnosis (most malignant portion of pathology specimen listed)	Mean PEM lesion-to-background ratio	Result	Invasive tumor size at pathology (if malignant)
1	Benign	1.95	TN	
2	Fibroadenoma	1.59	TN	
3	Ductal hyperplasia	2.19	TN	
4	Apocrine metaplasia	1.30	TN	
5	Typical hyperplasia	2.78	FP	
6a[a]	Ductal hyperplasia	1.32	TN	
6b[a]	Invasive ductal carcinoma	7.70	TP	30 mm
7	Mild ductal hyperplasia	2.27	TN	
8	Atypical lobular hyperplasia	1.48	TN	
9	Sclerosing adenosis	2.03	TN	
10	Fibroadenoma	1.38	TN	
11	Fibroadenoma, sclerosing adenosis	2.53	TN	
12	Ductal carcinoma in situ, microinvasion	3.22	TP	1 mm
13[b]	Invasive lobular carcinoma	1.97	FN	10 mm
14	Invasive ductal carcinoma	3.50	TP	7 mm
15	Ductal carcinoma in situ, microinvasion	3.33	TP	1 mm
16	Invasive ductal carcinoma	2.63	TP	11 mm
17	Invasive mucinous carcinoma	5.29	TP	10 mm

In 2003, Del Guerra *et al.* [46] presented YAP-PEM prototype composed of two planar, stationary detectors of 30 x 30 cerium doped yttrium aluminium perovskite YAlO$_3$:Ce (YAP:Ce) finger crystals each having a dimension of 2 mm x 2 mm x 30 mm. The active area of the detector heads are 6 cm x 6 cm. The separation between the

detectors, axial FOV dimension, can be varied 5 cm to 10 cm (Figure 3.14). PSPMTs are chosen as photosensors of YAP-PEM. Energy resolution of the system is simulated as 25% at 511 keV, which agrees with value measured with YAP-PET. MC simulations showed that the proposed scanner is able to detect tumors down to 0.065 cm^3, when positioned in the center of the FOV (SNR = 10:1). It is also shown that the reduction of the width of the energy window decreases the SNR, so the lowest energy threshold is used which is 50 keV and the upper threshold is set to be 650 keV. The simulations also confirmed the importance of the compression by showing that at a compression of 5 cm, a tumor of size 0.065 cm^3 was detectable with a good SNR of 8.7±1.0. A tumor of size 0.5 cm^3 was detectable at a distance of 1 cm from the center of the FOV.
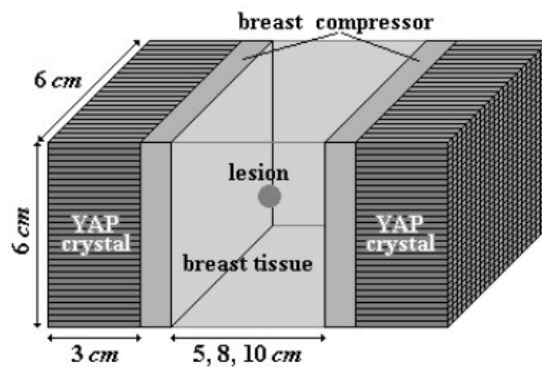
Figure 3.14 YAP-PEM prototype by Del Guerra *et al.* [46].

Motta *et al.* [47] presented another Monte Carlo study of YAP-PEM prototype in 2004, where the relationship between the SNR and the tumor size, width of the energy window, compressor distance and distance from the center are clearly shown (Figure 3.15).
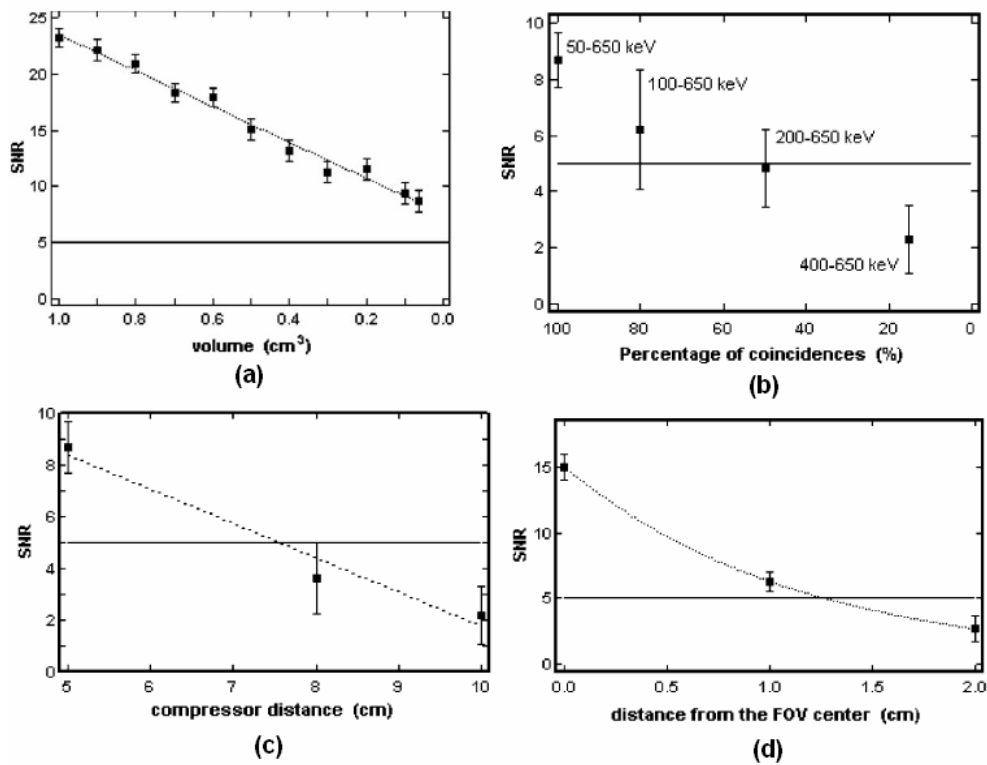
Figure 3.15 Performance measurements of YAP-PEM **(a)** Tumor volume vs. SNR, **(b)** Width of energy window vs. SNR, **(c)** Compressor distance vs. SNR, **(d)** Distance from the FOV center vs. SNR [47].

In the year of 2004, Belcari *et al.* [48] evaluated the performance the YAP-PEM system by uniform irradiation. The photosensors of the system are a 3 x 3 array of Hamamatsu R8520-C12 with an area of 25.7 mm x 25.7 mm, which has an active area of 22 mm x 22 mm (Figure 3.16). When the detector is irradiated with a ^{22}Na source and only the crystals that are facing the active area of a tube are identified, the mean FWHM of the pixel image is measured to be 0.9 mm. But if the flood field image is obtained with 511 keV photons and using a 3 mm quartz window, where pixels facing the active area are covered with black tape and the others are left open, pixel FWHM is found to be 1.4 mm.
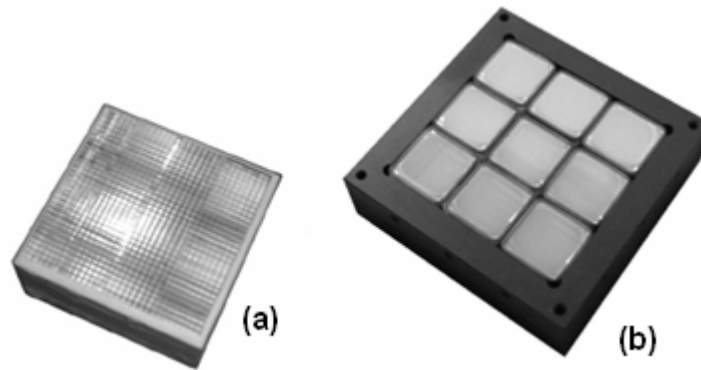
Figure 3.16   Components of YAP-PEM prototype **(a)** A photograph of YAP:Ce crystal matrix, **(b)** A photograph of 9 PSPMTs [48].

In the years of 2004 and 2005, Karimian *et al.* [49,50] proposed a cylindrical breast imager for the patients in prone position. In CYBPET an individual breast hangs from the body and covered by a thin plastic to make a mild pressure and is positioned in the center FOV, where the rest of the body is shielded properly. The CYBPET consists of 6912 BGO crystals, each having dimensions of 3.0 mm transaxial, 5.0 mm axial and 20 mm radial and grouped in detector blocks of 8 x 8 crystals. Each detector block has 32 rings and a transaxial-axial FOV of 17.0 cm with a ring diameter of 22 cm. The crystals are coupled directly to APDs. The energy threshold is set to 400 keV and the minimum tangential and radial resolution for the system is found to be 2.8 mm by performing simulations using PETSIM. The maximum tangential and radial resolutions are found to be 3.2 mm and 3.4 mm, respectively.

4. MONTE CARLO SIMULATIONS

Monte Carlo methods are a widely used class of computational algorithms for simulating the behavior of various physical and mathematical systems which are too complicated to solve analitically. These methods are based on generating random numbers and observing that fraction of the numbers obeying some property or properties.

In our study, GRIT, BUILDER and DETECT2000 Monte Carlo simulation programs are used, which are developed by Tri-University Meson Facility (TRIUMF) detector group.

4.1 GRIT

GRIT is the first module of the simulation platform. GRIT stands for "Gamma-Ray Interaction Tracking". Using this program, the Compton and photoelectric interactions of gamma-rays produced by a point or spherical source of a specified geometry are simulated. The energy of the gamma-rays, type and dimensions of the scintillation crystals can be specified by the user. GRIT determines how the gamma-rays deposit their energy in the scintillator and generates an interaction list file as output, which is accordance with the syntax of the program DETECT. The output files contains the scintillation coordinates in x, y and z directions, the number of light photon generated, the index of the interaction (0 for photoelectric interaction or starting from 0 increases for each sequential Compton scatter for each gamma-ray) and x and y coordinates of the source location. This file is used as the input file of the program BUILDER for the next steps of the simulation [51].

4.2 BUILDER

BUILDER is a utility for managing model geometry definitions for input to the light transport simulation DETECT2000, specialized in the modeling of detectors for PET.

BUILDER is the interface between the user's model definition and the DETECT simulation driver. Sophisticated detectors like cylindrical or rectangular PMTs, block or continuous detectors can be designed by the user by connecting simple box components. Once each component is defined, BUILDER connects them, checking for overlaps and incompatible surface finishes, and then translates these higher level definitions into the lower level language DETECT can understand [52].

4.3   DETECT2000

DETECT is a Monte Carlo model of the behavior of optical systems with a special emphasis on scintillation detectors. It generates individual scintillation photons in specified portions of the scintillator, follows each photon in its passage through the various components and interactions with surfaces, allows for the possible absorption and re-emission by a wave-shifting component, and records the fate (absorption, escape, or detection) of each. In addition to its ultimate fate, decay and delay times, total elapsed time to detection, number of reflecting surfaces encountered, last coordinates and whether or not the photon was wavelength shifted are recorded for each photon traced.

A very general syntax for geometry specification exists to allow the representation of complex systems consisting of composites of many different scintillator and/or wave-shifting elements. Any one element may consist of a volume specified by multiple planar, cylindrical, conical, or spherical surfaces with arbitrary orientation. More complex shapes can be built up by with "pseudo-surfaces" that are ignored by the simulation. The optical behavior of real surfaces may be specified to simulate possible reaction under polished, ground, painted, or metalized conditions. Surfaces in optical contact are treated using Snell's law of refraction. Within each optical element, bulk absorption, scattering, and wavelength shifting are simulated by specifying a mean distance of photon travel for each process. All these processes are wavelength dependent in DETECT2000.

The program uses initial definition statements to specify the optical properties of all materials and surface finishes used in the system. Abstract geometrical objects, planes,

cylinders, cones and spheres in convex or concave orientations are also defined. Components are then built out of these materials, finishes and objects. The optical behavior of each surface is chosen by selecting one of a set of previously defined surface finishes, including a photosensor surface representing the photocathode of a photomultiplier tube. Surfaces may either be external (assumed to be an interface with a vacuum) or shared with another component. An extensive set of consistency checks are incorporated to flag errors where possible.

Photons are isotropically generated within a defined material and volume subset of the system, a delay before emission being associated with the photon where the user has specified the probability distribution function (PDF) for that material. Photons are tracked on an individual basis until they are absorbed, detected, or have escaped from the system. At each photon reaction or scattering, the program logic determines the new direction of the photon, identifies the component in which it is traveling, and computes the next intersection with a surface. A random sampling is then made to determine if the photon is bulk absorbed, scattered, or wavelength shifted over this path. If none of these processes occur, the optical properties of the next surface determine whether the photon is reflected, refracted, detected, or absorbed. This process is then repeated for all subsequent paths in the history. A maximum flight time per history is specified to abort those cases in which a photon becomes internally trapped. In order to simulate the photosensor response time, a delay before detection is recorded for photons intersecting with detection type surfaces. In the absence of a user specified PDF, the delay is zero. After the specified number of histories have been completed, a report is prepared that summarizes the probability of occurrence and statistical uncertainty estimate of each of these possible fates.

Finally, data are reported on the detector response, the probability of wavelength shift, mean age (where age includes any scintillation decay time and photosensor response time), and mean number of surfaces encountered. This data is tabulated both for all photons and for just the subset that are ultimately detected. A histogram of photon ages can also be generated [53].
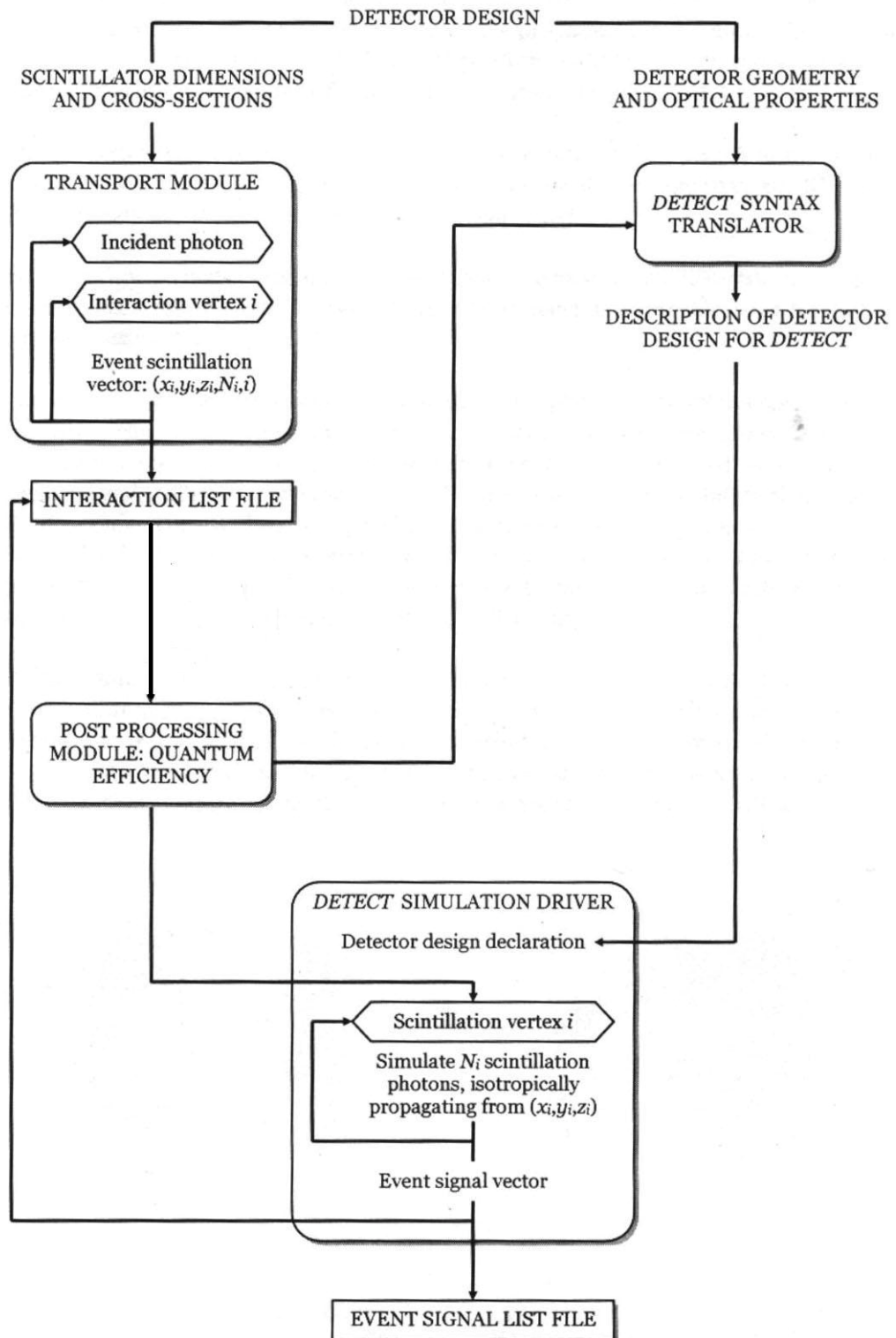
Figure 4.1 Flow diagram of the simulations [15].

5. NEURAL NETWORKS

The brain is a highly complex, nonlinear and parallel information-processing system. For certain computations, like pattern recognition, perception and motor control. It has the capability to organize its structural constituents, known as neurons, to perform certain computations. Although the most dramatic development of the human brain takes place during the first two years from birth, the development continues beyond that stage [54].

A developing neuron means a plastic brain: Plasticity permits the developing nervous system to adapt to the environment. Plasticity appears to be essential also for the neural networks whose structural constituents are "artificial neurons". A neural network is a structure that is designed to model the way in which the brain performs a particular task. To achieve good performance, neural networks employ a massive interconnection of simple computing neurons. Learning is attained through modification of synaptic weights between the neurons which is called "learning algorithm". A neural network resembles the brain in two aspects [54]:

(i) Knowledge is acquired by the network from its environment through a learning process.

(ii) Interneuron connection strengths, known as synaptic weights, are used to store the acquired knowledge.

Advantages of using neural networks are [54]:

(i) Nonlinearity,
(ii) Input-output mapping,
(iii) Adaptivity,
(iv) Evidential response,
(v) Contextual information,

(vi) Fault tolerance,

(vii) Very-large-scale integration (VLSI) implementability,

(viii) Uniformity of analysis and design,

(ix) Neurobiological analogy.

The structural elements of neural networks are neurons and these have three basic elements (Figure 5.1) [54]:

(i)   A set of synapses or connecting links, each of which is characterized by a weight or strengths of its own. Specifically, a signal x_j at the input of synapse j connected to neuron k is multiplied by the synaptic weight w_{kj}. Unlike a synapse in the brain, the synaptic weight of an artificial neuron may lie in a range that includes negative as well as positive values.

(ii) An adder for summing the input signals, weighted by the respective synapses of the neuron; the operations described here constitute a linear combiner.

(iii) An activation function for limiting the amplitude of the output of a neuron. The activation function is also referred to as a squashing function in that it limits the permissible amplitude range of the output signal to some finite value.
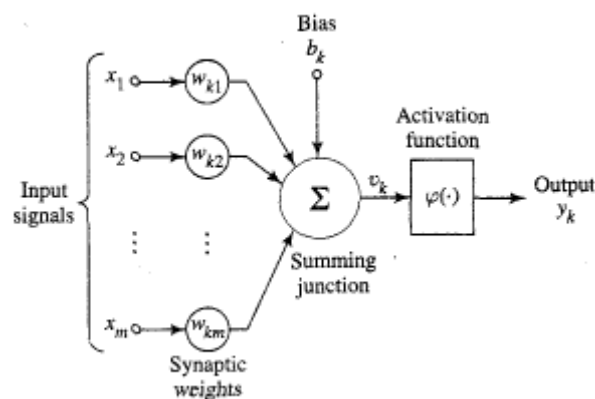
Figure 5.1 Nonlinear model of a neuron [54].

Figure 5.1 also includes an applied bias, b_k. The bias is used to increase or lower the net input of the activation function, depending on whether it is positive or negative, respectively.

The mathematical description of a neuron k can be made through the following equation:

$$u_k = \sum_{j=1}^{m} \omega_{kj} x_j \qquad (5.1)$$

and

$$y_k = \varphi\left(u_k + b_k\right) \qquad (5.2)$$

where x_1, x_2,......, x_m are the input signals; ω_{k1}, ω_{k2}, ..., ω_{km} are the synaptic weights of neuron k; u_k is the linear combiner output due to the input signals; b_k is the bias; $\varphi(.)$ is the activation function; and y_k is the output signal of the neuron. The use of bias b_k has the effect of applying an affine transformation to the output u_k of the linear combiner as shown by

$$v_k = u_k + b_k \qquad (5.3)$$

where v_k is called the induced local field or activation function of neuron k.

The activation function, denoted by $\varphi(v)$, defines the output of a neuron in terms of the induced local field v. Here we identify three basic types of activation functions (Figure 5.2):

(i)   Threshold Function:

$$\varphi(v)=\begin{cases}1 & if\ v\geq0\\0 & if\ v<0\end{cases} \tag{5.4}$$

Correspondingly, the output of neuron k employing such a threshold function is expressed as:

$$y_k=\begin{cases}1 & if\ v\geq0\\0 & if\ v<0\end{cases} \tag{5.5}$$

(ii)   Piecewise-Linear Function:

$$\varphi(v)=\begin{cases}1, & v\geq+\dfrac{1}{2}\\[2mm] v, & +\dfrac{1}{2}>v>-\dfrac{1}{2}\\[2mm] 0, & v\leq-\dfrac{1}{2}\end{cases} \tag{5.6}$$

(iii)   Sigmoid Function:

$$\varphi(v)=\frac{1}{1+\exp(-av)} \tag{5.7}$$

where a is the slope parameter of the sigmoid function. Hyperbolic tangent function is also used as an activation function:

$$\varphi(v)=\tanh(v) \tag{5.8}$$
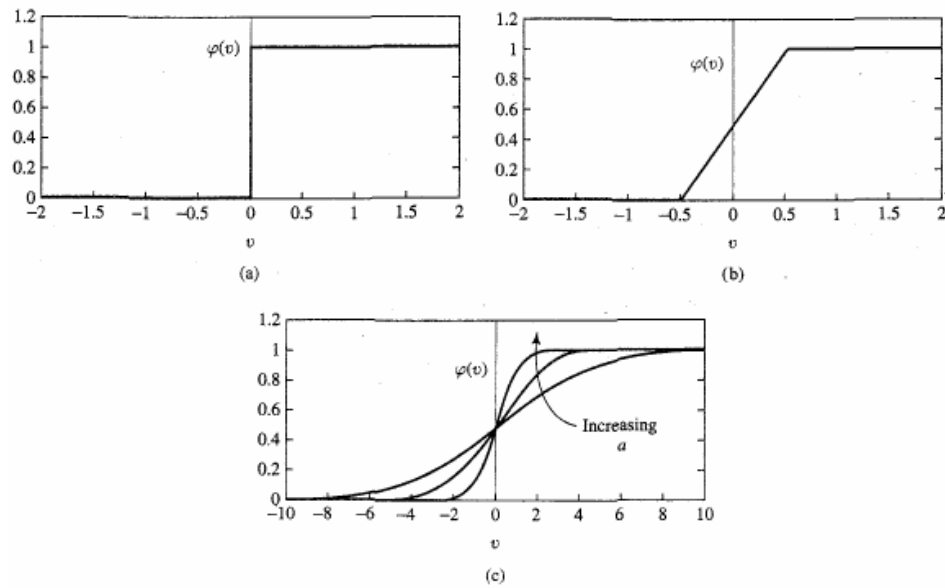
Figure 5.2 Basic types of threshold functions **(a)** Threshold function, **(b)** Piecewise-linear function, **(c)** Sigmoid function [54].

In this work, an important class of neural networks, *multilayer perceptrons (MLP)* are used, which are described in detail in the following sections of this chapter.

MLPs (Figure 5.3) typically consist of the input layer, one or more hidden layers and an output layer of computation nodes. They are applied to solve difficult problems in a supervised manner with an algorithm called *error back-propagation* algorithm. This algorithm is based on error correction learning rule, which can be seen as a generalization of the least-mean-square (LMS) algorithm.
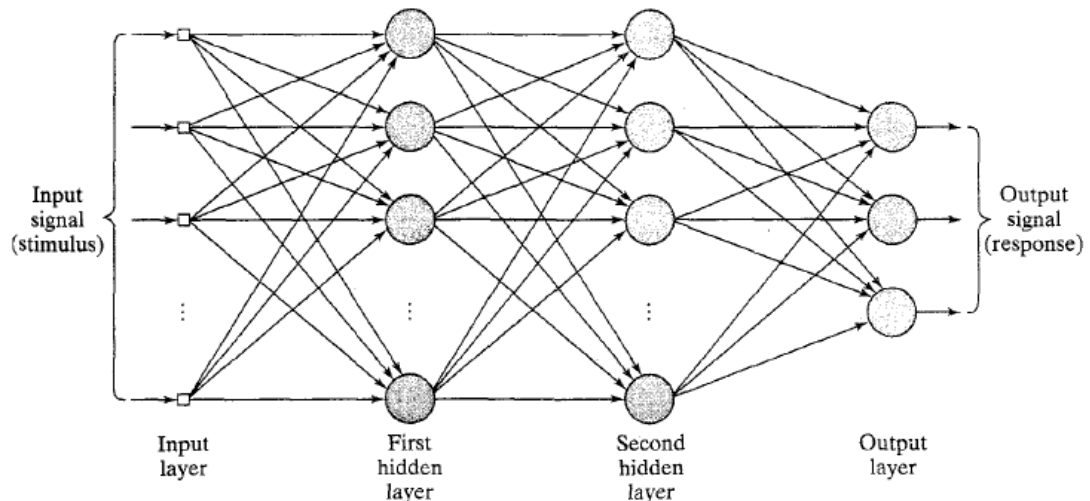
Figure 5.3 Architectural graph of an MLP with two hidden neurons [54].

In a MLP, there are two kins of signals identified:

(i)   *Function signals*. A function signal is an input signal (stimulus), propagates through the network and emerges at the output end of the network as an output signal.

(ii) *Error signals*. An error signal originates at an output neuron of the network and propagates backwards through the network.

Each hidden or output neuron of a MLP performs two computations:

(i)   The computation of the function signal appearing at the output of a neuron, which is expressed as a continuous nonlinear function of the input signal and synaptic weights associated with that neuron.

(ii) The computation of an estimate of the gradient vector (gradients of the error surface with respect to the weights connected to the inputs of a neuron), which is needed for the backward pass through the network.

The error signal at the output of neuron j at iteration n is defined by

$$e_j(n) = d_j(n) - y_j(n), \quad \text{neuron j is an output node} \tag{5.9}$$

The instantaneous value of the total error energy for neuron j is the sum of all error energies over all neurons in the output layer as follows

$$\varepsilon(n) = \frac{1}{2} \sum_{j \in C} e_j^2(n) \tag{5.10}$$

The averaged squared error energy is obtained by summing ε(n) over all n and then normalizing with respect to the set size N, as shown by

$$\varepsilon_{av} = \frac{1}{N} \sum_{n=1}^{N} \varepsilon(n) \tag{5.11}$$

For a giving training set, ε$_{av}$ represents the *cost function* as a measure of learning performance. The objective of the learning process is to adjust the free parameters of the network to minimize ε$_{av}$ by adjusting the weights on a *pattern-by-pattern* basis until one epoch (one complete presentation of the entire training set). The adjustments to the weights are made according to the errors computed for each pattern presented to the network.

The induced local field $v_j(n)$ produced at the in put of the activation function associated with neuron j is therefore

$$v_j(n) = \sum_{i=0}^{m} \omega_{ji}(n) y_i(n) \tag{5.12}$$

where m is the total number of inputs applied to neuron j. The synaptic weight ω$_{j0}$ equals the bias b$_j$ applied to the neuron j. So, the function signal appearing at the output of neuron j at iteration n is

$$y_j(n) = \varphi(v_j(n)) \tag{5.13}$$

Like in the LMS algorithm, the correction Δω$_{ji}$(n) to the synaptic weight is proportional to the partial derivative $\partial\varepsilon(n) / \partial\omega_{ji}(n)$, which represents a sensitivity factor, determining the direction of search in weight space for the synaptic weight ω$_{ji}$.

$$\frac{\partial\varepsilon(n)}{\partial\omega_{ji}(n)} = \frac{\partial\varepsilon(n)}{\partial e_j(n)} \frac{\partial e_j(n)}{\partial y_j(n)} \frac{\partial y_j(n)}{\partial v_j(n)} \frac{\partial v_j(n)}{\partial\omega_{ji}(n)} \tag{5.14}$$

Differentiating both sides of Eq. 5.10 with respect to $e_j(n)$, we get

$$\frac{\partial \varepsilon(n)}{\partial e_j(n)} = e_j(n) \tag{5.15}$$

Differentiating both sides of Eq. 5.9 with respect to $y_j(n)$, we get

$$\frac{e_j(n)}{\partial y_j(n)} = -1 \tag{5.16}$$

Next, differentiating Eq. 5.13 with respect to $v_j(n)$, we get

$$\frac{\partial y_j(n)}{\partial v_j(n)} = \varphi'_j(v_j(n)) \tag{5.17}$$

Finally, differentiating Eq. 5.12 with respect to $\omega_{ji}(n)$ yields

$$\frac{\partial v_j(n)}{\partial \omega_{ji}(n)} = y_i(n) \tag{5.18}$$

The use of Eqs. 5.15, 5.18 in 5.14 yields

$$\frac{\partial \varepsilon(n)}{\partial \omega_{ji}(n)} = -e_j(n)\varphi'_j(v_j(n))y_i(n) \tag{5.19}$$

The correction $\Delta\omega_{ji}(n)$ applied to $\omega_{ji}(n)$ is defined by the delay rule:

$$\Delta\omega_{ji}(n) = -\eta \frac{\partial \varepsilon(n)}{\partial \omega_{ji}(n)} \tag{5.20}$$

where η is the learning-rate parameter of the back-projection algorithm. Accordingly, the use of Eqs. 5.19 and 5.20 yields

$$\Delta\omega_{ji}(n) = \eta\,\delta_j(n)\,y_i(n) \tag{5.21}$$

where the local gradient $\delta_j(n)$ is defined by

$$\delta_j(n) = -\frac{\partial\varepsilon(n)}{\partial v_j(n)}$$

$$= -\frac{\partial\varepsilon(n)}{\partial e_j(n)}\frac{\partial e_j(n)}{\partial y_j(n)}\frac{\partial y_j(n)}{\partial v_j(n)} \tag{5.22}$$

$$= e_j(n)\varphi_j'(v_j(n))$$

From Eqs. 5.21 and 5.22, it is clearly seen that a key factor for the calculation of $\Delta\omega_{ji}(n)$ is the error signal $e_j(n)$ at the output of the neuron j. So, two different cases must be identified according to the location of neuron j. In one case it is an output node and in the other it is a hidden node.

Neuron j is an output node.   The computation of the error signal for an output node is done, see Eq. 5.9. Having determined $e_j(n)$, the local gradient $\delta_j(n)$ can be easily computed using Eq. 5.22.

Neuron j is a hidden node.   If neuron j is located in a hidden layer, there is no output signal specified to it. The error signal cannot be computed directly, so the development of the back-propagation algorithm gets complicated.
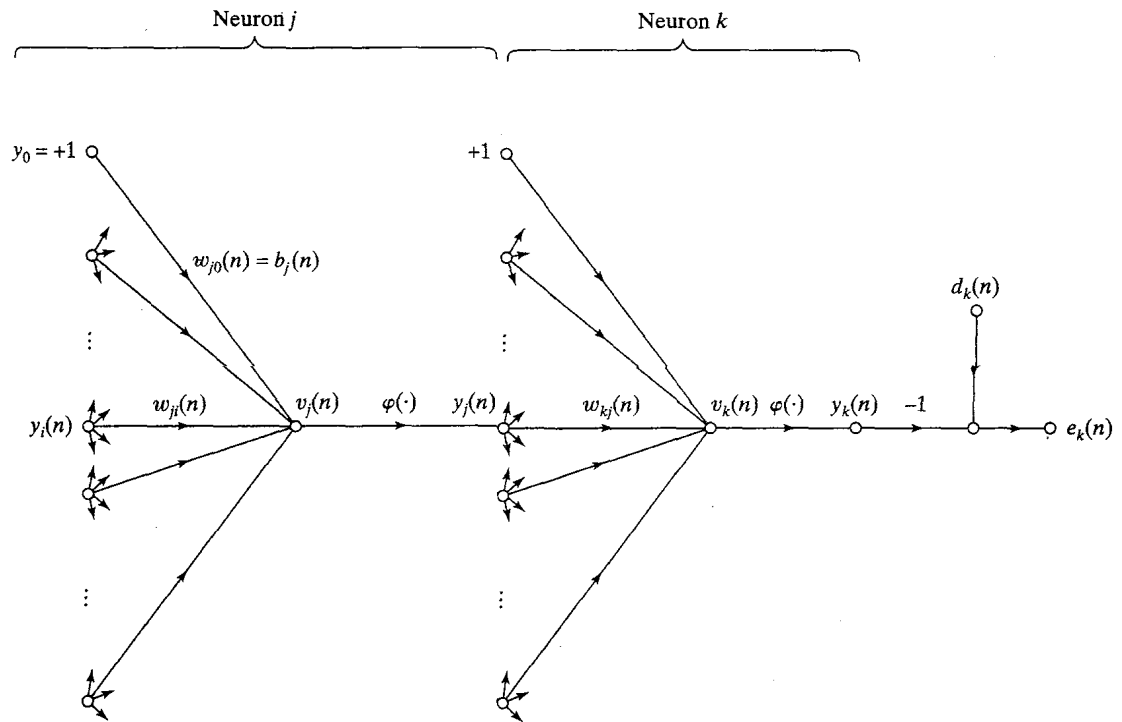
Figure 5.4 Signal-flow graph showing the details of output neuron k to hidden neuron j [54].

According to the Eq. 5.22, the local gradient of hidden neuron j can be computed as

$$\delta_j(n) = -\frac{\partial \varepsilon(n)}{\partial y_j(n)} \frac{\partial y_j(n)}{\partial v_j(n)}$$

$$= -\frac{\partial \varepsilon(n)}{\partial y_j(n)} \varphi_j'(v_j(n)), \quad \text{neuron j is hidden} \tag{5.23}$$

where in the second line the Eq. 5.17 is used. To calculate the partial derivative $\partial \varepsilon(n) / \partial y_j(n)$, we may proceed as follows. From Fig. 5.4, it is seen that

$$\varepsilon(n) = \frac{1}{2} \sum_{k \in C} e_k^2(n), \quad \text{neuron k is an output node} \tag{5.24}$$

Differentiating Eq. 5.24 with respect to the function signal $y_j(n)$, we get

$$\frac{\partial \varepsilon(n)}{\partial y_j(n)} = \sum_k e_k \frac{\partial e_k(n)}{\partial y_j(n)} \qquad (5.25)$$

Rewriting the Eq. 5.25

$$\frac{\partial \varepsilon(n)}{\partial y_j(n)} = \sum_k e_k(n) \frac{\partial e_k(n)}{\partial v_k(n)} \frac{\partial v_k(n)}{\partial y_j(n)} \qquad (5.26)$$

From Fig. 5.4, we note that k is an output neuron and $e_k(n)$ can be calculated easily.

$$e_k(n) = d_k(n) - y_k(n)$$

$$= d_k(n) - \varphi_k(v_k(n)), \quad \text{neuron k is an output node} \qquad (5.27)$$

Hence,

$$\frac{\partial e_k(n)}{\partial v_k(n)} = -\varphi'_k(v_k(n)) \qquad (5.28)$$

For neuron k, the induced local field is calculated as

$$v_k(n) \approx \sum_{j=0}^{m} \omega_{kj}(n) \, y_j(n) \qquad (5.29)$$

where m is the total number of inputs (excluding the bias) applied to neuron k. Here again, the synaptic weight $\omega_{k0}(n)$ is equal to the bias $b_k(n)$ applied to neuron k corresponding input is fixed at the value +1. Differentiating the Eq. 5.29 with respect to $y_j(n)$ yields

$$\frac{\partial v_k(n)}{\partial y_j(n)} = \omega_{kj}(n) \tag{5.30}$$

By using Eqs. 5.28, 5.30 in 5.26 we get

$$\frac{\partial \varepsilon(n)}{\partial y_j(n)} = -\sum_k e_k(n)\varphi_k'(v_k(n))\,\omega_{kj}(n) \tag{5.31}$$

$$= -\sum_k \delta_k(n)\,\omega_{kj}(n)$$

Finally, using Eq. 5.31 in 5.23, we get the back-propagation formula fro the local gradient $\delta_j(n)$ as described:

$$\delta_j(n) = \varphi_j'(v_j(n))\sum_k \delta_k(n)\omega_{kj}(n), \quad \text{neuron j is hidden} \tag{5.32}$$

To summarize, the correction $\Delta\omega_{ji}(n)$ applied to the synaptic weight connecting neuron i to neuron j is defined by the delta rule:

$$\begin{pmatrix} Weight \\ correction \\ \Delta\omega_{ji}(n) \end{pmatrix} = \begin{pmatrix} learning-rate \\ parameter \\ \eta \end{pmatrix} \cdot \begin{pmatrix} local \\ gradient \\ \delta_j(n) \end{pmatrix} \cdot \begin{pmatrix} input\ signal \\ of\ neuron\ j \\ y_i(n) \end{pmatrix} \tag{5.33}$$

In the application of the back-propagation algorithm, there are two distinct passes. The first pass is the *forward* pass and the second one is the *backward* pass. In the forward pass, the synaptic weights are not altered through out the network and the function signals of the network are computed on a neuron-by-neuron basis. On the other hand, the backward pass starts at the output layer and propagates leftward toward the input layer and the error signals are used to compute the local gradient of each neuron. This recursive process permits the synaptic weights of the network to undergo changes in accordance with the delta rule according to the Eq. 5.33.

6. METHODOLOGY AND RESULTS

In our simulations, we designed a continuous LSO detector with a detection surface area of 49 mm x 49 mm [25]. The thickness of the scintillator varies between 3 mm and 24 mm with increments of 3 mm. The photodetector to which the LSO coupled is Hamamatsu 8500 multi-anode PMT (MAPMT) and has a 8 x 8 matrix of anodes [25]. The pixel size of each anode is 5.8 mm x 5.8 mm. The total effective area of the MAPMT is 49 mm x 49 mm, which is 88.79% of the overall active area (Figure 6.1). A borosilicate glass window of thickness of 1.5 mm is modeled between the crystal and the detection surface of the MAPMT.
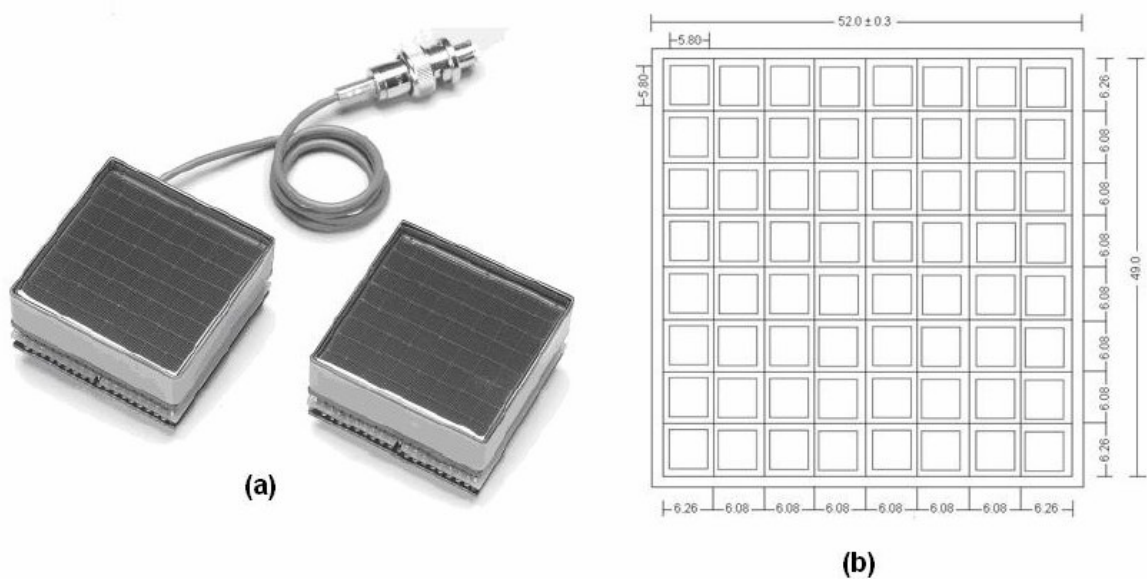
Figure 6.1 Hamamatsu H8500 Flat Panel MAPMT **(a)** Left: H8500, Right: H8500B [55], **(b)** Detailed top view of the PMT (units in mm).

Optical properties of surfaces and detector components are modeled in BUILDER, choosing painted for side surfaces and ground for face surfaces. Reflection coefficient for ground face is set to 0.95 and for painted sides it is set to 0.85. LSO crystal and glass are modeled to have index of refraction of 1.82 and 1.52, respectively.

For each crystal thickness, two groups of simulations are performed. The first group is used to train our ANN and the second group is done to test the performance of our network. Taking into account the symmetry of our system, the simulations are performed only for the first quadrant of our detector covering an area of 24 mm x 24 mm (Figure 6.2).
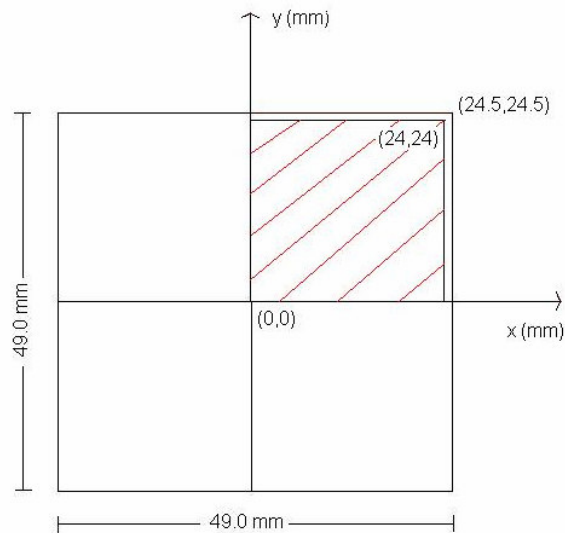
Figure 6.2 Simulated LSO crystal (49 mm x 49 mm), the photons are sent to the first quadrant of the crystal according to the symmetry properties of the detector.

During the generation of our training set, the selected area is divided into a 24 x 24 grid with a pixel size of 1 mm x 1 mm. A narrow beam of 100 photons of 511 keV energy are sent to each grid point from 50 mm away from the crystal surface. To prepare the test data, the area is divided into a 5 x 5 grid with pixel sizes of 6 mm x 6 mm and to each grid point, 1000 photons (again of 511 keV energy) are sent from 50 mm away. This procedure is repeated for every detector configuration of different crystal thickness. An energy threshold of 350 keV is applied to the data, in order to eliminate a portion of the Compton scatter events, where these energy threshold values are in agreement with the literature [10,46]. Signals detected from each anode are weighted according to the locations of the anodes and 64 outputs from the anodes are reduced 4 [25].

The energy resolution obtained from our simulations is 12.2% for a crystal thickness of 15 mm. The quantum efficiency of our MAPMT is assumed to be 22.5%. The pulse height spectrum can be seen in Figure 6.3.
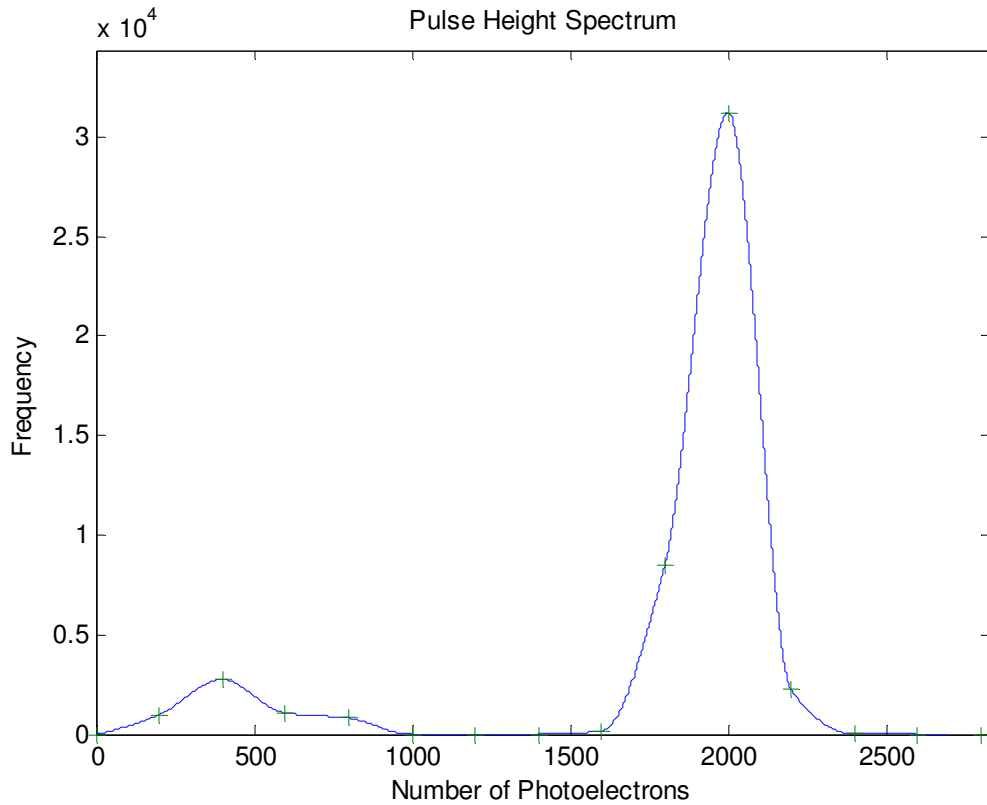
Figure 6.3 Pulse Height Spectrum of LSO for our detector for 511 keV photons.

Our MLP consists of one input layer of 4 neurons, two hidden layers with 15 and 8 neurons and an output layer of 1 neuron. The 4 neurons in the input layer correspond to the 4 MAPMT outputs and the neuron in the output layer corresponds to the x coordinate, which is tried to be estimated. The MLP code is written partially in Matlab and in C programming language.

In this work, an activation function of sigmoidal type (Eq. 5.7) is used, which satisfies the requirement of being differentiable, where the slope parameter is chosen as 1.

In order to make the trajectory of the weight space smoother, the learning rate parameter η is chosen small, namely as 0.1. Choosing η smaller provides the changes to the synaptic weights smaller. On the other hand, making η too large in order to speed up the learning, the resulting changes may cause the network to be unstable, namely oscillatory.

For the training of our network for all crystal thicknesses, the number of iterations is chosen to be 10000, for which the cost function for all crystal thicknesses reaches a saturation plateau.

In the following sections, resolution and bias values for all thicknesses for 350 keV energy threshold are summarized. For the calculation of optimal bin width of point spread functions for FWHM, Eq. 6.1 [56] is used.

$$w = 2 * iqr(x) * (size(x))^{-1/3},$$ (6.1)

where x is the vector of calculated x coordinates for the x value which is tried to be estimated and iqr(x) is the interquartile range of the values in x.

6.1 Results: Crystal Thickness is 3 mm

Table 6.1, 6.2 and 6.3 compares the bias and spatial resolution obtained with Anger algorithm and with MLP. The biases and resolutions are calculated using data of the test grid, corresponding to the same x coordinate (x=0, x=12 or x=24), which is tried to be estimated. Figure 6.4 and 6.5 are point spread functions obtained from Anger algorithm and MLP network for x=0, x=12 and x=24, respectively.
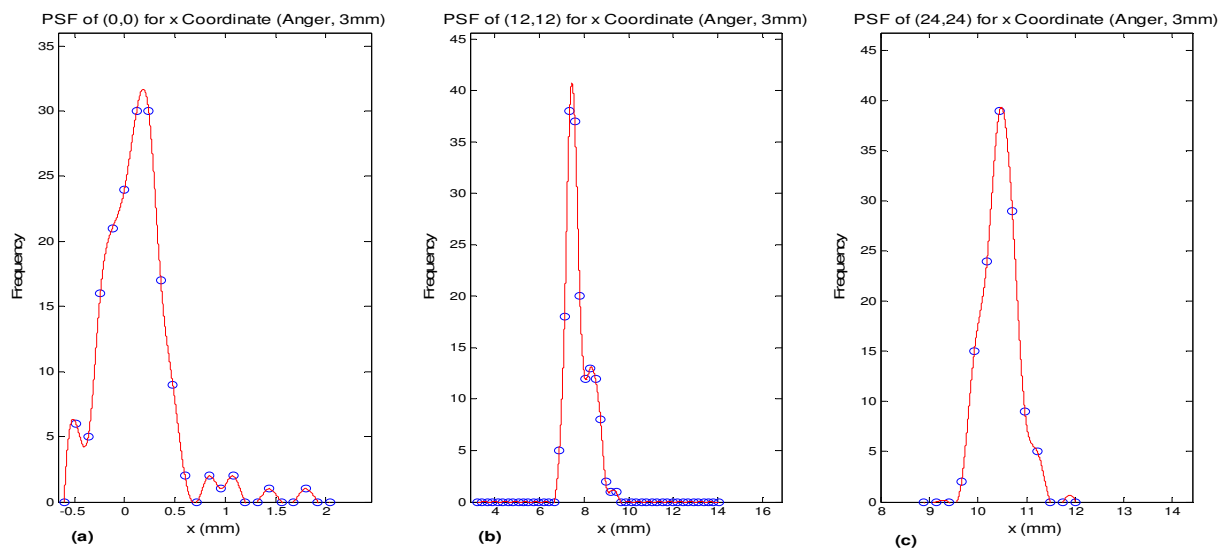
Figure 6.4 PSFs of Anger for crystal thickness 3 mm **(a)** for x =0, **(b)** for x=12 and **(c)** for x=24.
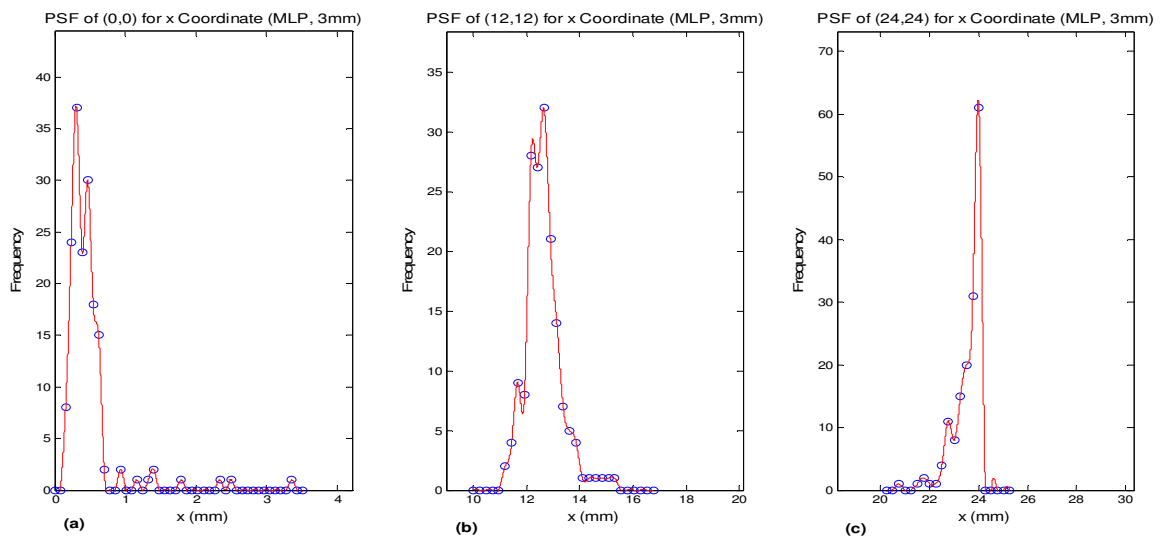
Figure 6.5 PSFs of MLP for crystal thickness 3 mm **(a)** for x =0, **(b)** for x=12 and **(c)** for x=24.

Table 6.1

Anger and MLP results for crystal thickness 3 mm for x = 0 at (0,0).

	Anger (350 keV)	MLP (350 keV)
Resolution (mm)	0.613	0.329
Bias (mm)	-0.186	-0.305

Table 6.2

Anger and MLP results for crystal thickness 3 mm for x = 12 at (12,12).

	Anger (350 keV)	MLP (350 keV)
Resolution (mm)	0.741	1.022
Bias (mm)	4.203	-0.647

Table 6.3

Anger and MLP results for crystal thickness 3 mm for x = 24 at (24,24).

	Anger(350 keV)	MLP(350 keV)
Resolution (mm)	0.742	0.382
Bias (mm)	13.523	0.010

6.2   Results: Crystal Thickness is 6 mm

Table 6.4, 6.5 and 6.6 compares the bias and spatial resolution obtained with Anger algorithm and with MLP. The biases and resolutions are calculated using data of the test grid, corresponding to the same x coordinate (x=0, x=12 or x=24), which is tried to be estimated. Figure 6.6 and 6.7 are point spread functions obtained from Anger algorithm and MLP network for x=0, x=12 and x=24, respectively.
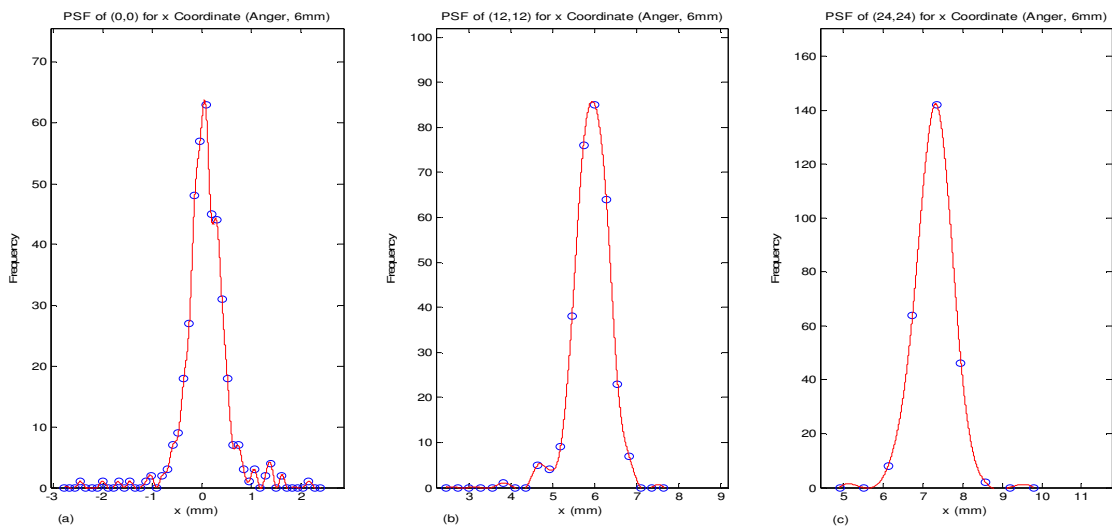
Figure 6.6 PSFs of Anger for crystal thickness 6 mm **(a)** for x =0, **(b)** for x=12 and **(c)** for x=24.
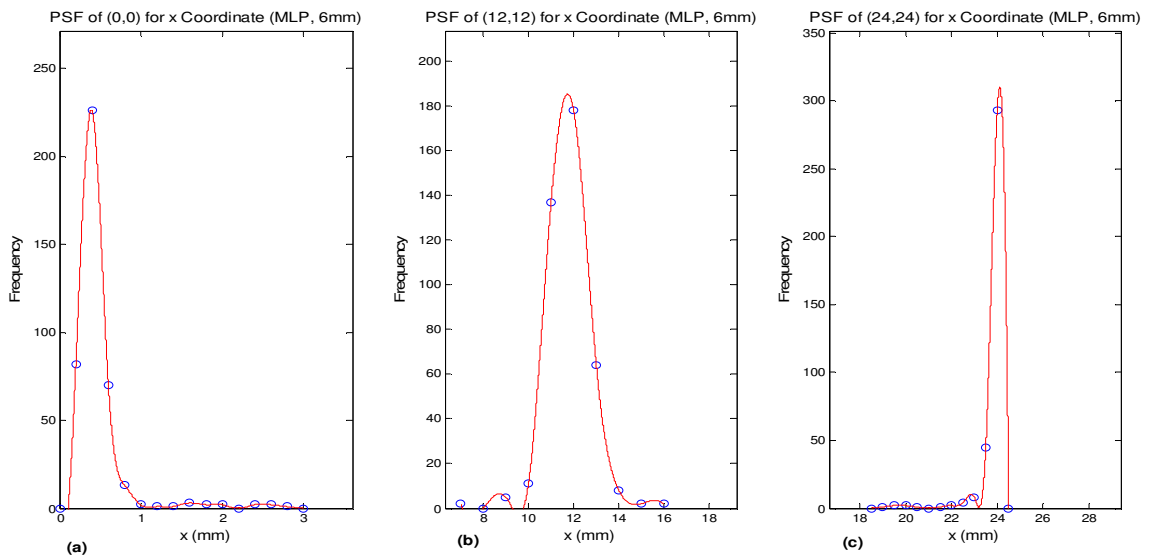
Figure 6.7 PSFs of MLP for crystal thickness 6 mm **(a)** for x =0, **(b)** for x=12 and **(c)** for x=24.

Table 6.4
Anger and MLP results for crystal thickness 6 mm for x = 0 at (0,0).

	Anger (350 keV)	MLP (350 keV)
Resolution (mm)	0.625	0.321
Bias (mm)	-0.059	-0.391

Table 6.5
Anger and MLP results for crystal thickness 6 mm for x = 12 at (12,12).

	Anger(350 keV)	MLP(350 keV)
Resolution (mm)	0.907	2.086
Bias (mm)	6.027	0.264

Table 6.6
Anger and MLP results for crystal thickness 6 mm for x = 24 at (24,24).

	Anger(350 keV)	MLP(350 keV)
Resolution (mm)	1.045	0.677
Bias (mm)	16.670	-0.112

6.3   Results: Crystal Thickness is 9 mm

Table 6.7, 6.8 and 6.9 compares the bias and spatial resolution obtained with Anger algorithm and with MLP. The biases and resolutions are calculated using data of the test grid, corresponding to the same x coordinate (x=0, x=12 or x=24), which is tried to be estimated. Figure 6.8 and 6.9 are point spread functions obtained from Anger algorithm and MLP network for x=0, x=12 and x=24, respectively.
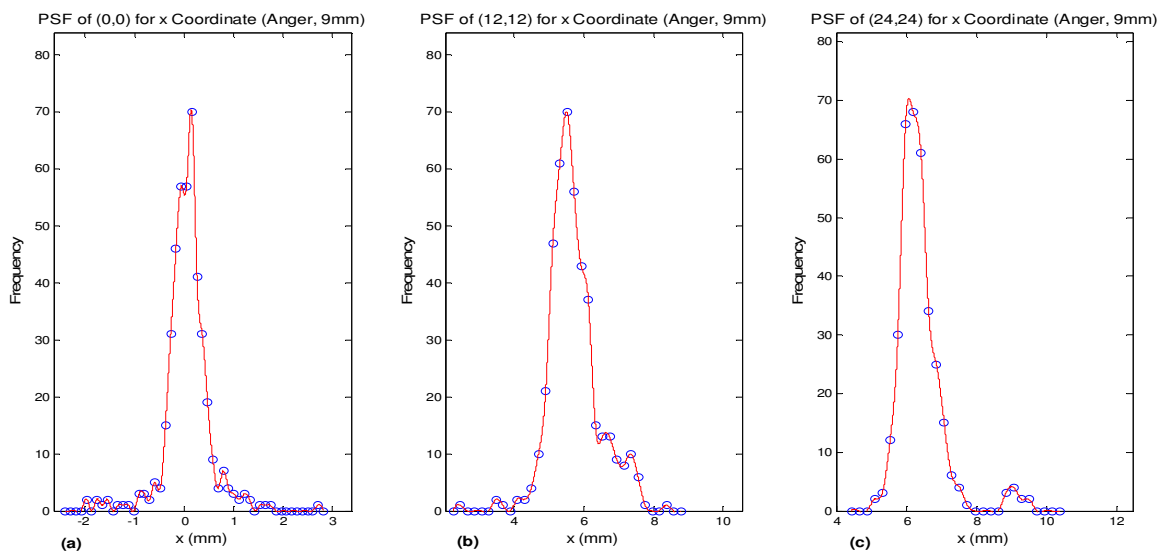
Figure 6.8 PSFs of Anger for crystal thickness 9 mm **(a)** for x =0, **(b)** for x=12 and **(c)** for x=24.
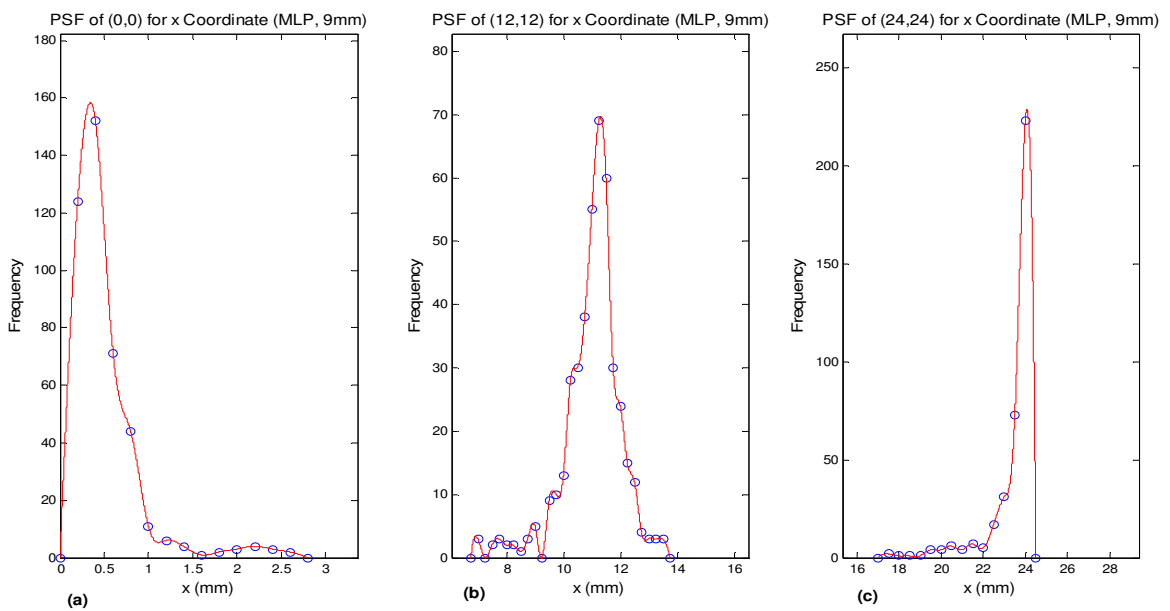
Figure 6.9 PSFs of MLP for crystal thickness 9 mm **(a)** for x =0, **(b)** for x=12 and **(c)** for x=24.

Table 6.7
Anger and MLP results for crystal thickness 9 mm for x = 0 at (0,0).

	Anger(350 keV)	MLP(350 keV)
Resolution (mm)	0.538	0.459
Bias (mm)	-0.146	-0.344

Table 6.8
Anger and MLP results for crystal thickness 9 mm for x = 12 at (12,12).

	Anger(350 keV)	MLP(350 keV)
Resolution (mm)	1.138	1.013
Bias (mm)	6.494	0.697

Table 6.9
Anger and MLP results for crystal thickness 9 mm for x = 24 at (24,24).

	Anger(350 keV)	MLP(350 keV)
Resolution (mm)	0.839	0.752
Bias (mm)	17.936	-0.081

6.4   Results: Crystal Thickness is 12 mm

Table 6.10, 6.11 and 6.12 compares the bias and spatial resolution obtained with Anger algorithm and with MLP. The biases and resolutions are calculated using data of the test grid, corresponding to the same x coordinate (x=0, x=12 or x=24), which is tried to be estimated. Figure 6.10 and 6.11 are point spread functions obtained from Anger algorithm and MLP network for x=0, x=12 and x=24, respectively.
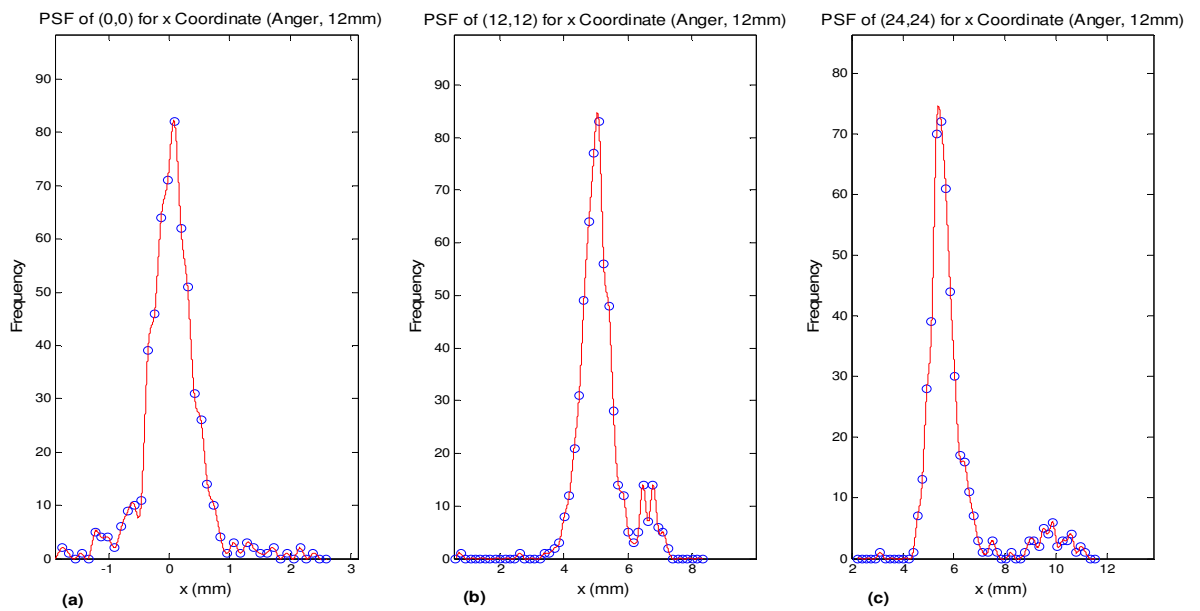
Figure 6.10 PSFs of Anger for crystal thickness 12 mm **(a)** for x =0, **(b)** for x=12 and **(c)** for x=24.

Figure 6.11 PSFs of MLP for crystal thickness 12 mm **(a)** for x =0, **(b)** for x=12 and **(c)** for x=24.

Table 6.10
Anger and MLP results for crystal thickness 12 mm for x = 0 at (0,0).

	Anger (350 keV)	MLP (350 keV)
Resolution (mm)	0.695	0.432
Bias (mm)	-0.072	-0.181

Table 6.11
Anger and MLP results for crystal thickness 12 mm for x = 12 at (12,12).

	Anger (350 keV)	MLP (350 keV)
Resolution (mm)	0.880	1.898
Bias (mm)	6.949	0.364

Table 6.12
Anger and MLP results for crystal thickness 12 mm for x = 24 at (24,24).

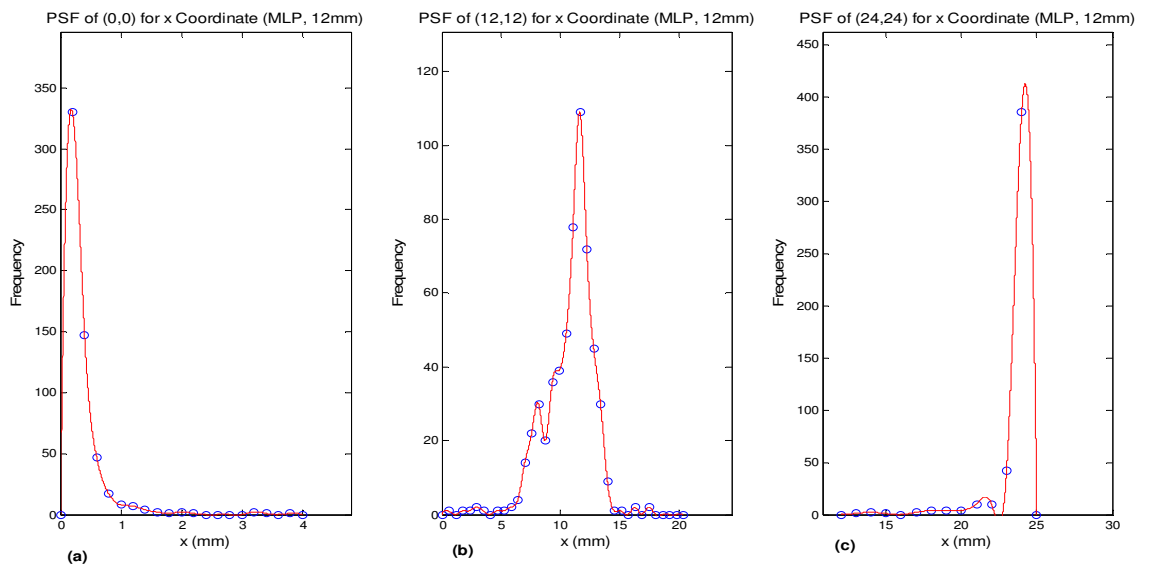|	Anger (350 keV)	MLP (350 keV)
Resolution (mm)	0.831	0.648
Bias (mm)	18.603	-0.126

6.5　Results: Crystal Thickness is 15 mm

Table 6.13, 6.14 and 6.15 compares the bias and spatial resolution obtained with Anger algorithm and with MLP. The biases and resolutions are calculated using data of the test grid, corresponding to the same x coordinate (x=0, x=12 or x=24), which is tried to be estimated. Figure 6.12 and 6.13 are point spread functions obtained from Anger algorithm and MLP network for x=0, x=12 and x=24, respectively.
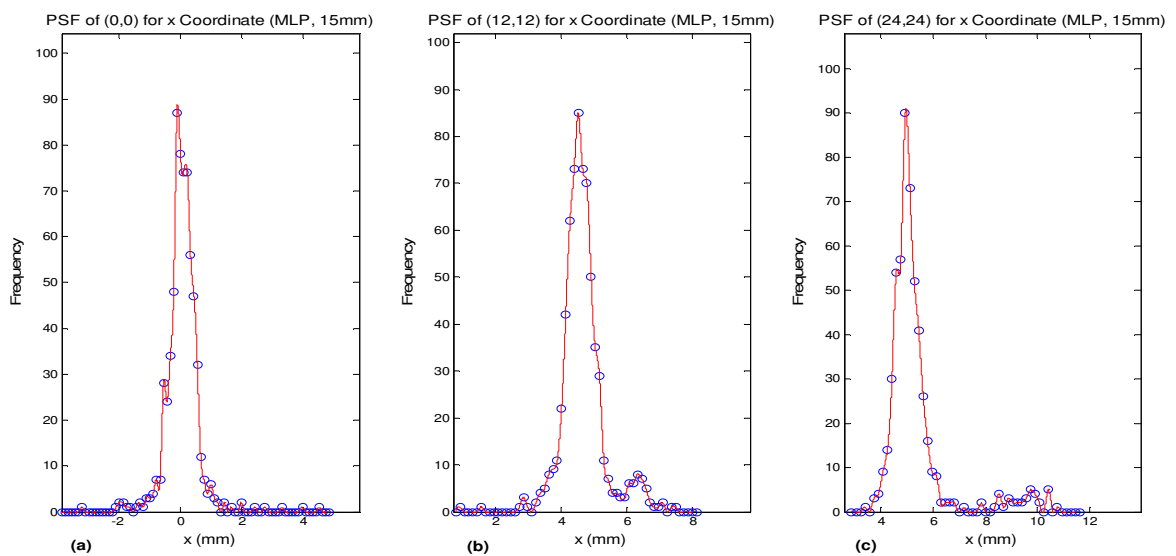
Figure 6.12 PSFs of Anger for crystal thickness 15 mm **(a)** for x =0, **(b)** for x=12 and **(c)** for x=24.
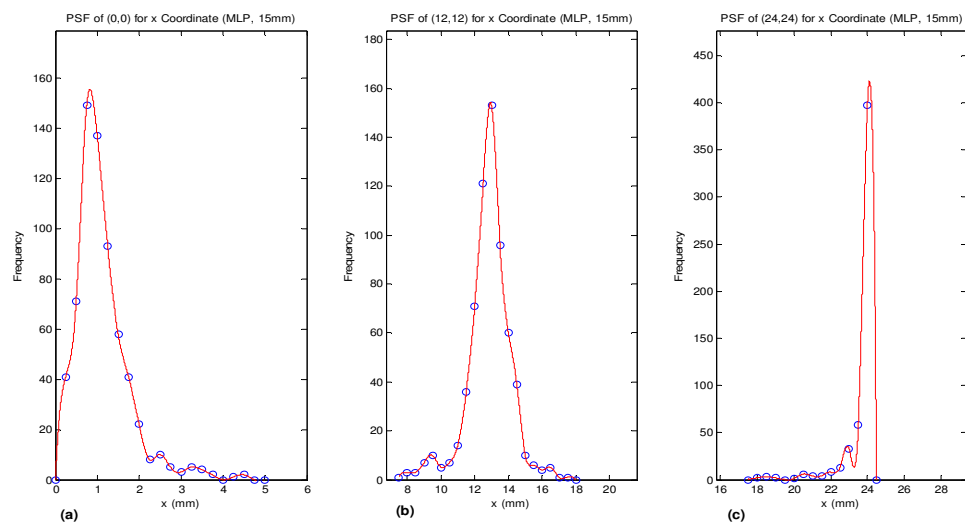
Figure 6.13 PSFs of Anger for crystal thickness 15 mm **(a)** for x =0, **(b)** for x=12 and **(c)** for x=24.

Table 6.13
Anger and MLP results for crystal thickness 15 mm for x = 0 at (0,0).

	Anger (350 keV)	MLP (350 keV)
Resolution (mm)	0.706	0.820
Bias (mm)	0.092	-0.829

Table 6.14
Anger and MLP results for crystal thickness 15 mm for x = 12 at (12,12).

	Anger (350 keV)	MLP (350 keV)
Resolution (mm)	0.861	1.626
Bias (mm)	7.478	-0.938

Table 6.15
Anger and MLP results for crystal thickness 15 mm for x = 24 at (24,24).

	Anger (350 keV)	MLP (350 keV)
Resolution (mm)	0.859	0.669
Bias (mm)	19.024	-0.117

6.6 Results: Crystal Thickness is 18 mm

Table 6.16, 6.17 and 6.18 compares the bias and spatial resolution obtained with Anger algorithm and with MLP. The biases and resolutions are calculated using data of the test grid, corresponding to the same x coordinate (x=0, x=12 or x=24), which is tried to be estimated. Figure 6.14 and 6.15 are point spread functions obtained from Anger algorithm and MLP network for x=0, x=12 and x=24, respectively.
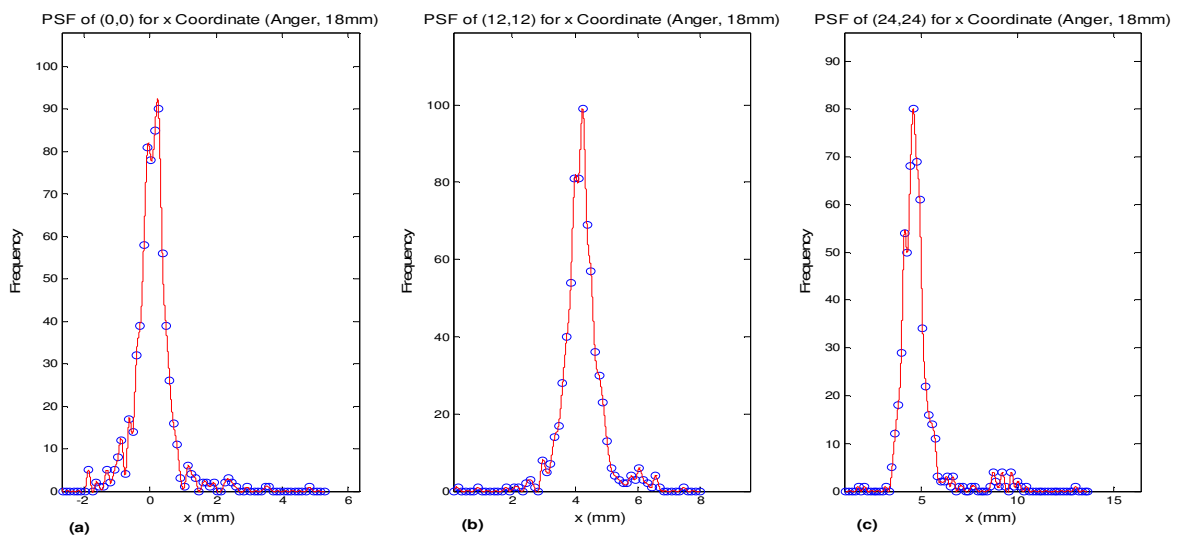
Figure 6.14 PSFs of Anger for crystal thickness 18 mm **(a)** for x =0, **(b)** for x=12 and **(c)** for x=24.
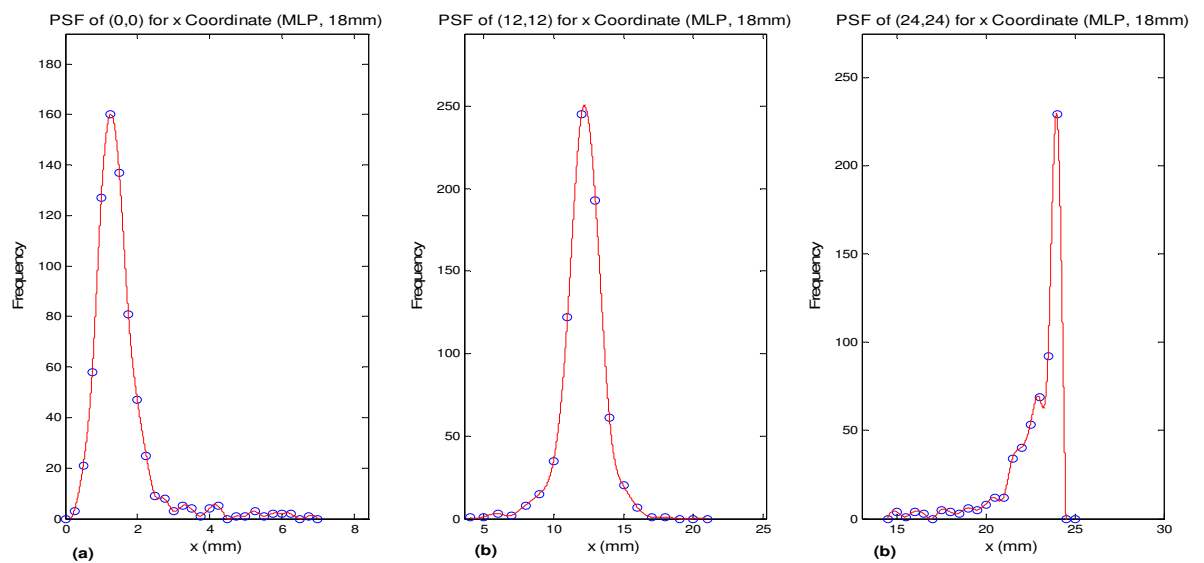
Figure 6.15 PSFs of Anger for crystal thickness 18 mm **(a)** for x =0, **(b)** for x=12 and **(c)** for x=24.

Table 6.16
Anger and MLP results for crystal thickness 18 mm for x = 0 at (0,0).

	Anger (350 keV)	MLP (350 keV)
Resolution (mm)	0.662	0.865
Bias (mm)	-0.227	-1.146

Table 6.17
Anger and MLP results for crystal thickness 18 mm for x = 12 at (12,12).

	Anger (350 keV)	MLP (350 keV)
Resolution (mm)	0.718	2.258
Bias (mm)	7.753	0.402

Table 6.18
Anger and MLP results for crystal thickness 18 mm for x = 24 at (24,24).

	Anger (350 keV)	MLP (350 keV)
Resolution (mm)	1.010	0.726
Bias (mm)	19.411	0.026

6.7   Results: Crystal Thickness is 21 mm

Table 6.19, 6.20 and 6.21 compares the bias and spatial resolution obtained with Anger algorithm and with MLP. The biases and resolutions are calculated using data of the test grid, corresponding to the same x coordinate (x=0, x=12 or x=24), which is tried to be estimated. Figure 6.16 and 6.17 are point spread functions obtained from Anger algorithm and MLP network for x=0, x=12 and x=24, respectively.
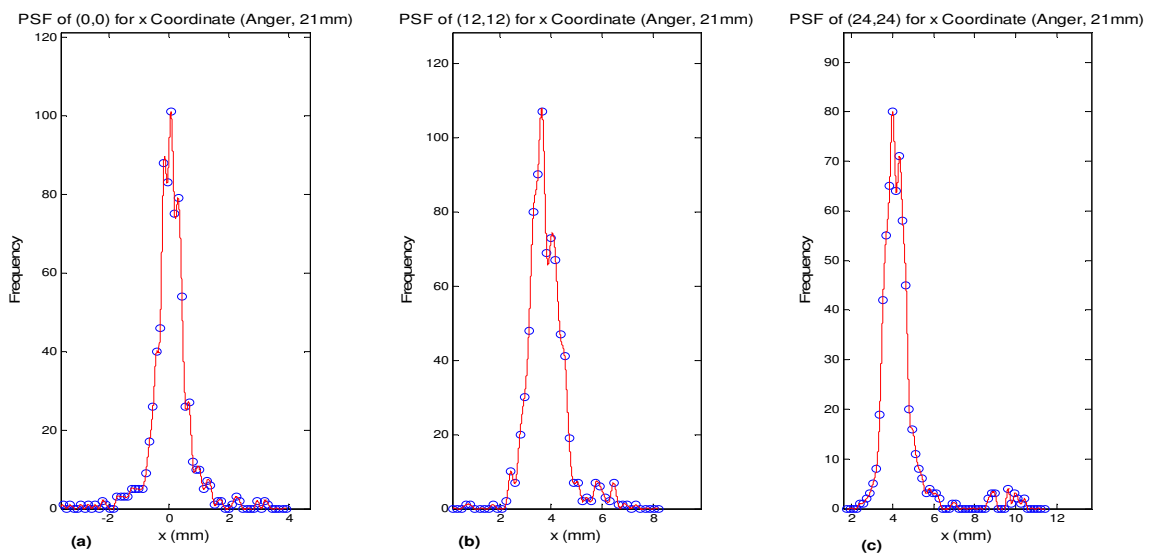
Figure 6.16 PSFs of Anger for crystal thickness 21 mm **(a)** for x =0, **(b)** for x=12 and **(c)** for x=24.
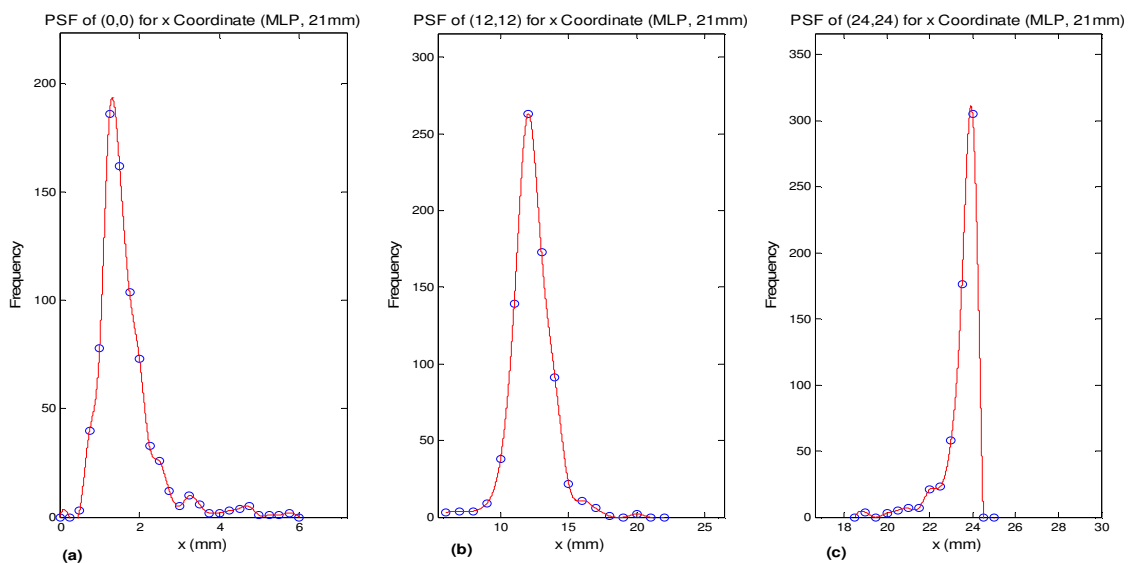
Figure 6.17 PSFs of MLP for crystal thickness 21 mm **(a)** for x =0, **(b)** for x=12 and **(c)** for x=24.

Table 6.19
Anger and MLP results for crystal thickness 21 mm for x = 0 at (0,0).

	Anger (350 keV)	MLP (350 keV)
Resolution (mm)	0.719	0.753
Bias (mm)	0.066	1.318

Table 6.20
Anger and MLP results for crystal thickness 21 mm for x = 12 at (12,12).

	Anger (350 keV)	MLP (350 keV)
Resolution (mm)	1.021	2.487
Bias (mm)	8.350	-0.045

Table 6.21
Anger and MLP results for crystal thickness 21 mm for x = 24 at (24,24).

	Anger (350 keV)	MLP (350 keV)
Resolution (mm)	1.172	0.841
Bias (mm)	19.991	0.069

6.8 Results: Crystal Thickness is 24 mm

Table 6.22, 6.23 and 6.24 compares the bias and spatial resolution obtained with Anger algorithm and with MLP. The biases and resolutions are calculated using data of the test grid, corresponding to the same x coordinate (x=0, x=12 or x=24), which is tried to be estimated. Figure 6.18 and 6.19 are point spread functions obtained from Anger algorithm and MLP network for x=0, x=12 and x=24, respectively.
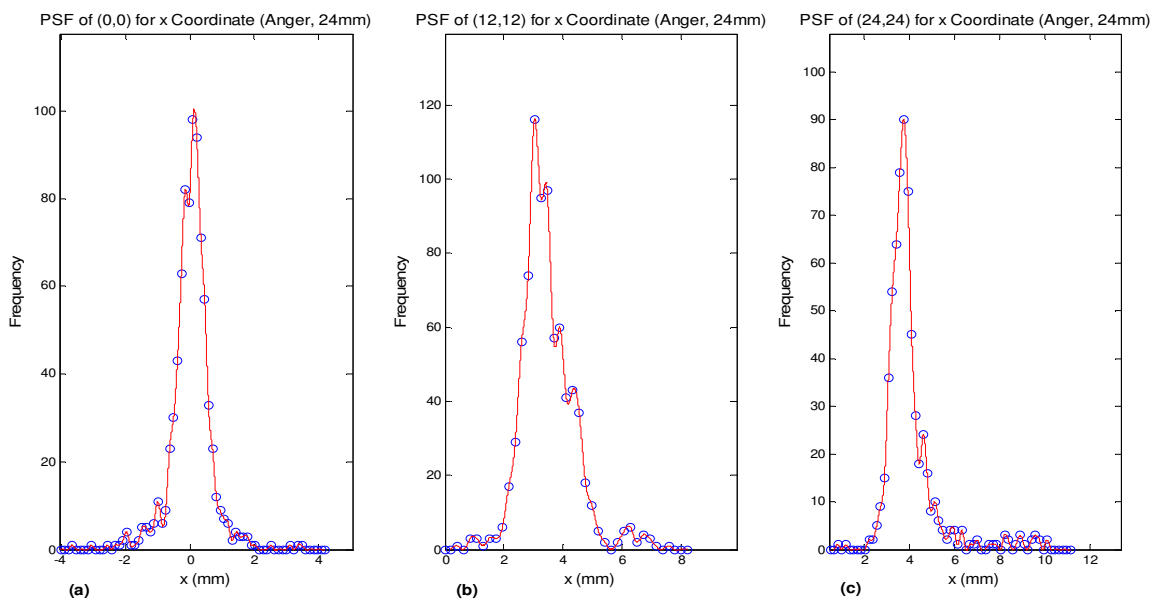
Figure 6.18 PSFs of Anger for crystal thickness 24 mm **(a)** for x =0, **(b)** for x=12 and **(c)** for x=24.
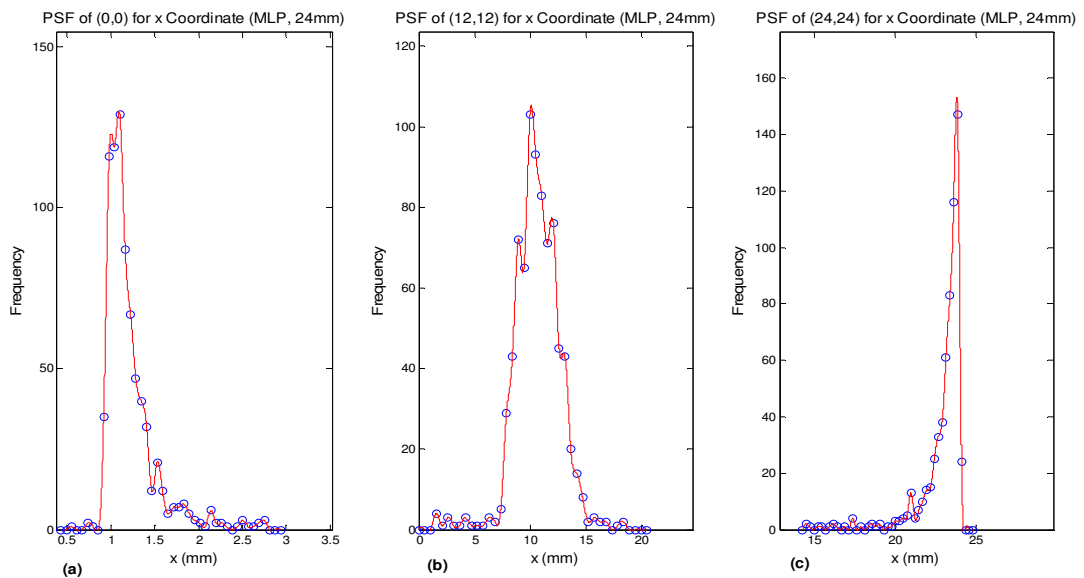
Figure 6.19 PSFs of MLP for crystal thickness 24 mm **(a)** for x =0, **(b)** for x=12 and **(c)** for x=24.

Table 6.22
Anger and MLP results for crystal thickness 24 mm for x = 0 at (0,0).

	Anger (350 keV)	MLP (350 keV)
Resolution (mm)	0.835	0.690
Bias (mm)	0.139	1.091

Table 6.23
Anger and MLP results for crystal thickness 24 mm for x = 12 at (12,12).

	Anger (350 keV)	MLP (350 keV)
Resolution (mm)	1.153	3.894
Bias (mm)	8.957	1.921

Table 6.24
Anger and MLP results for crystal thickness 24 mm for x = 24 at (24,24).

	Anger (350 keV)	MLP (350 keV)
Resolution (mm)	0.951	0.698
Bias (mm)	20.240	0.181

6.9   Summary of Results

FWHM values calculated using Anger algorithm are corrected using bias maps for thickness (Figure 6.20 and Figure 6.21) and the results are plotted in Figure 6.22. Table 6.25 and Table 6.26 compares FWHMs calculated with unbiased Anger and MLP.
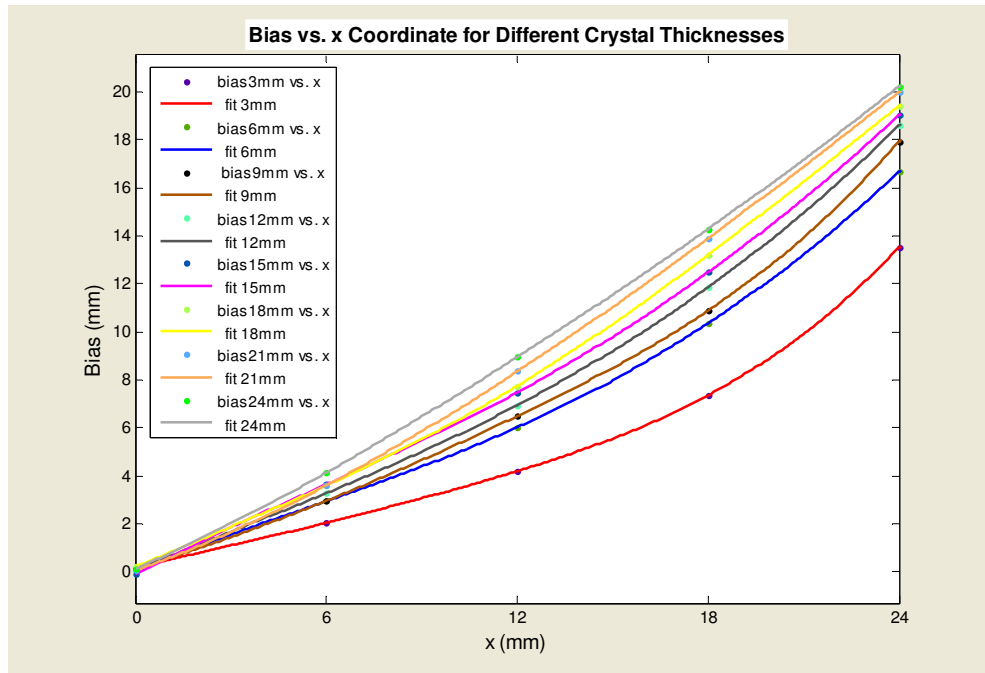
Figure 6.20 Bias for different crystal thicknesses vs. x coordinates for Anger algorithm.
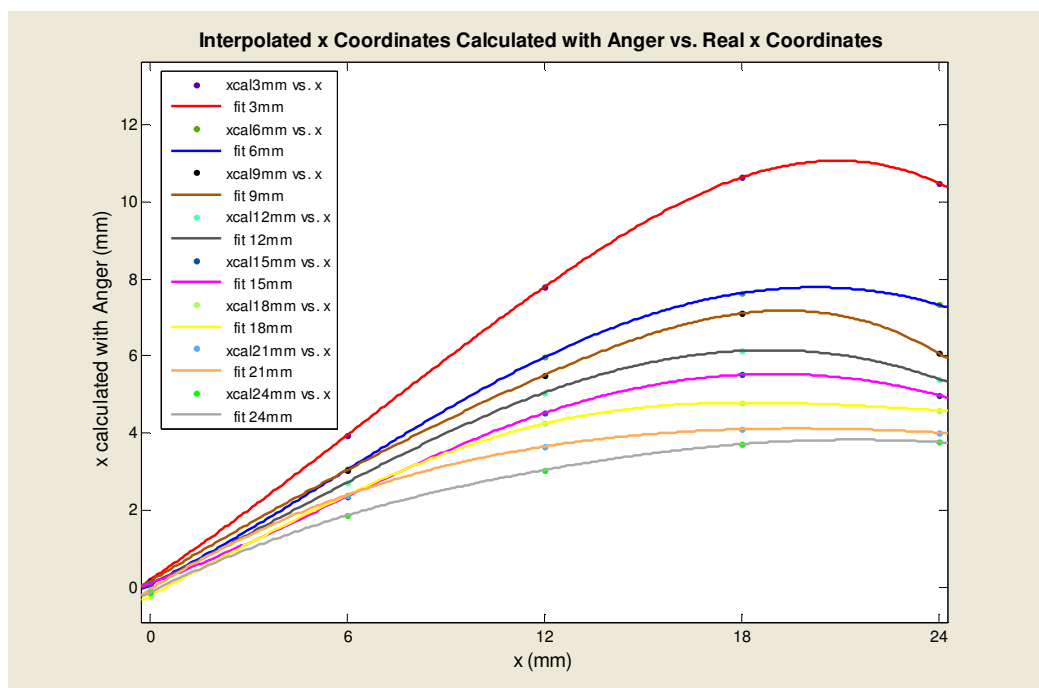
Figure 6.21 Interpolated x coordinates with Anger algorithm vs. x coordinates.

Table 6.25
Spatial resolutions calculated for the test point (0,0) with unbiased Anger and MLP.

LSO thickness (mm)	Anger (Unbiased) Resolution (mm)	MLP Resolution (mm)
3	0.910	0.329
6	1.200	0.321
9	0.930	0.459
12	1.520	0.432
15	1.520	0.820
18	1.700	0.865
21	1.730	0.753
24	2.490	0.690

Table 6.26
Spatial resolutions calculated for the test point (12,12) with unbiased Anger and MLP.

LSO thickness (mm)	Anger (Unbiased) Resolution (mm)	MLP Resolution (mm)
3	1.170	1.022
6	2.710	2.086
9	2.860	1.013
12	2.780	1.898
15	2.840	1.626
18	3.410	2.258
21	4.470	2.487
24	4.780	3.894
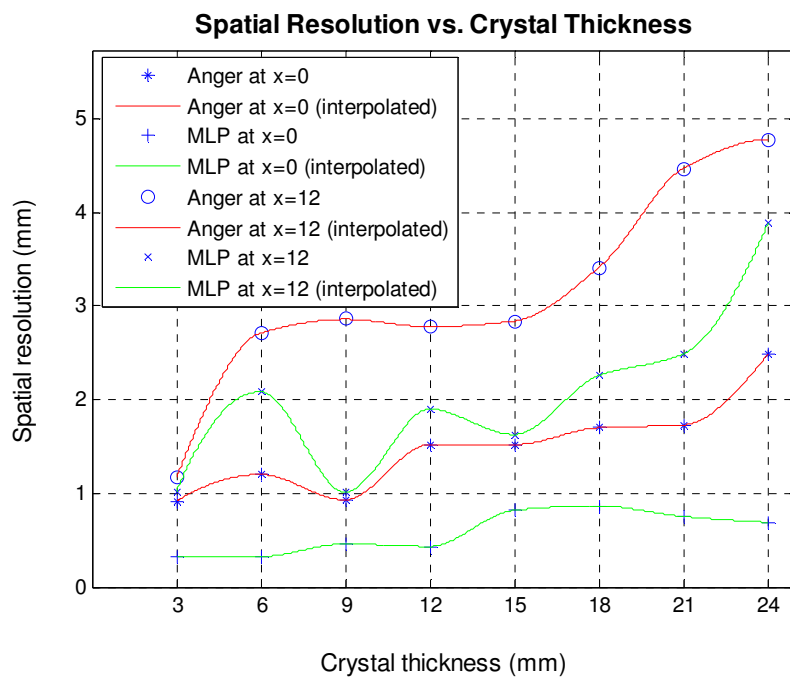
Figure 6.22 Spatial resolution vs. crystal thickness at x=0 and x=12.
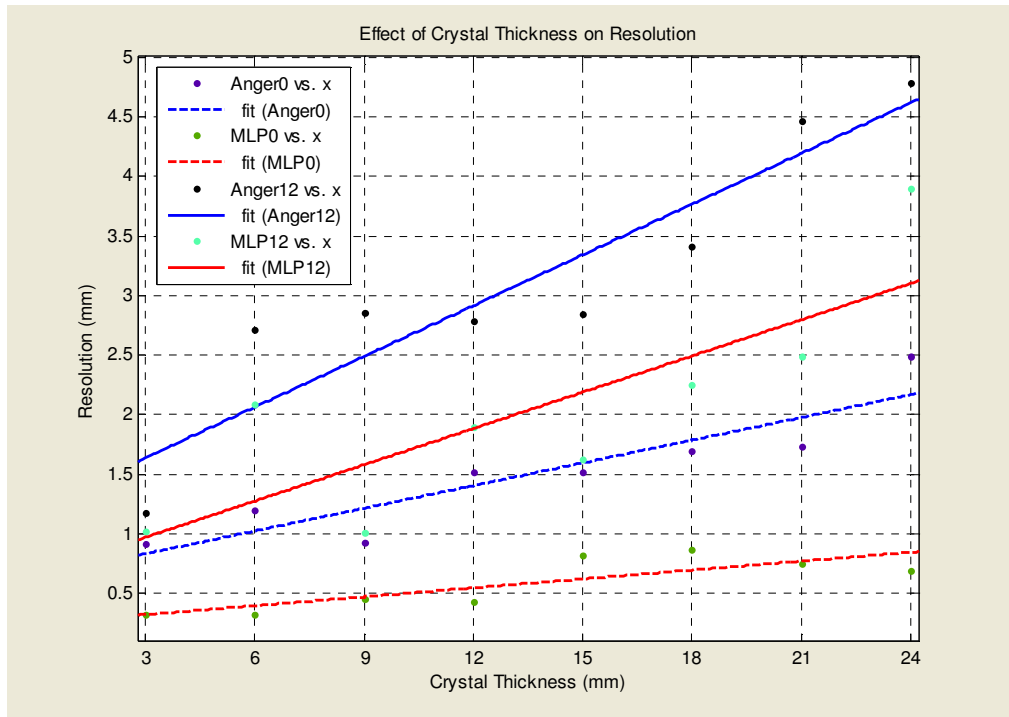
Figure 6.23 Effect of crystal thickness on spatial resolution for Anger algorithm and MLP.

On Figure 6.23, the spatial resolution data points for both algorithms are fitted to linear curves for each crystal thickness, in order to investigate the effect of crystal thickness on the degradation on spatial resolution.

The attenuation for a gamma ray is calculated according the Eq. 2.12, where the linear attenuation coefficient of LSO for gamma rays of 511 keV energy is 0.86 cm^{-1} [57]. The crystal efficiencies are calculated according to the attenuation and the percentage of interactions used due to the energy threshold. Crystal efficiencies according to the varying crystal thickness are shown in Table 6.27 and in Figure 6.23.

Table 6.27
Crystal thickness vs. crystal efficiency.

LSO thickness (mm)	No energy threshold Efficiency (%)	Energy Threshold=350 keV Efficiency (%)
3	17.96	10.93
6	39.83	30.75
9	53.78	40.71
12	61.50	55.37
15	73.05	63.45
18	77.48	69.45
21	82.92	73.13
24	86.61	65.28
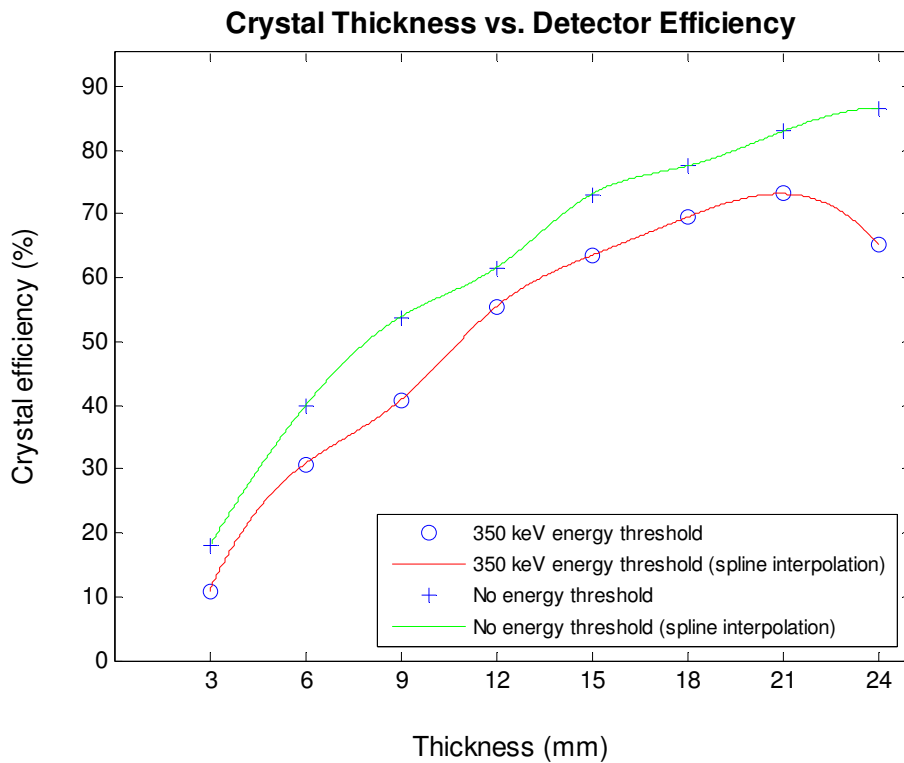
Figure 6.24 Crystal thickness vs. crystal efficiency with no energy threshold and 350 keV energy thresholds.

DISCUSSION AND CONCLUSION

For this work, a MAPMT of 8 x 8 anodes is coupled to crystals, which has different thicknesses varying from 3 mm to 24 mm. A MLP of two hidden layers is used, which have 15 and 8 neurons, respectively. The 64 outputs of the MAPMT is reduced to 4, in order to simplify the electronics of the real system, so the input layer consists of 4 neurons corresponding to the output vectors of the MAPMT and the output layer has one neuron for the estimated coordinate.

In this study, the crystal thickness has been varied and the performance parameters like spatial resolution and bias of a PET detector are compared and significantly better results are obtained with MLP when compared with Anger algorithm (Figure 6.22). This result shows that usage of thick scintillation crystals for small PEM detectors.

The spatial resolution got worse in the center of the FOV (12,12) because of the high-reflective side painting, which is chosen in order not to sacrifice the sensitivity of the detector and count statistics, but caused the photons reflect towards the center of the crystal and caused the light distribution to distort in the edges of the detector. This degradation can be compensated as a future work by using a more absorptive side painting, by training the network with more events per each grid position and by optimizing the network parameters, such as number of hidden layers and number of neurons in the hidden layers, for each crystal thickness. Moreover, the output of each anode can be used separately to feed the network, instead of decreasing the number from 64 to 4.

From Figure 6.23, it can be seen that both for (x = 0) and (x =12), the fitted curves have steeper slopes for Anger algorithm, meaning that it is more sensitive to changes in crystal thickness. This result reveals that the degradation in spatial resolution is less when an MLP is utilized for positioning. It is observed that there is a trade-off between sensitivity and crystal thickness for Anger algorithm. Since we obtained better results in spatial resolution using MLP based algorithm even for thick crystals, the sensitivity is not sacrificed.

Among the crystal thicknesses utilized in the study, the worst results for the average resolution, the resolution at the center point of the crystal and at the point (12,12) are obtained for a crystal thickness of 24 mm. Moreover, the usage of crystals thicker than 24 mm results in excessive Compton scatters, which are eliminated by applying an energy threshold. But Figure 6.24 reveals that the efficiency of the crystal starts to decrease after 21 mm which is a consequence of energy thresholding.

The systematic error of the Anger algorithm is again shown in this thesis, therefore it is proven once more that new approaches for scintillation positioning are needed for electronically practical, time efficient and real-time applications. It can be clearly seen that increasing the crystal thickness results in more compression and the compression near the edges of the crystal is more than the compression in the center of the crystal.

A simplification can be done by training the different regions of the crystal with different networks allowing the usage of simpler neural networks and shortening the training times.

The gamma photons simulated in this work are sent perpendicularly to the crystal surface. For depth-of-interaction information, the training can be done also for oblique photon incidences.

Another prospective research can be the use of higher energy thresholds (400-450 keV) for this detector configuration and investigate the effect on the crystal efficiency and the spatial resolution.

REFERENCES

1. Phelps, M. E., *PET Molecular Imaging and Its Biological Applications*, New York: Springer Science+Business Media, 2004.

2. Murthy, K., M. Aznar, C.J. Thompson, A. Loutfi, R. Lisbona and J.H. Gagnon , "Results of Preliminary Clinical Trials of the Positron Emission Mammography System PEM-I: A Dedicated Breast Imaging System Producing Glucose Metabolic Images Using FDG," *J Nucl Med*, Vol. 41, pp. 1851-1858, Nov 2000.

3. Edward A., L., R. Freimanis, N.D. Perrier, K. Morton, N.M. Lesko, S. Bergman, K. Geisinger, R.C. Williams, C. Sharpe, V. Zavarsin, I.N. Weinberg, P.Y. Stepanov, D. Beylin, K. Lauckner, M. Doss, J. Lovelace and L.P. Adler, "Positron Emission Mammography: Initial Clinical Results," *Annals of Surgical Oncology*, Vol. 10, pp. 86-91, 2003.

4. Valk, P. E., D. L. Bailey, D. W. Townsend and M. N. Maisey, *Positron Emission Tomography: Basic Science and Clinical Practice*, London: Springer, 3rd ed., 2004.

5. First positron imaging device. Available: http://www.mit.edu/~glb/.

6. Phelps, M. E., ed., *PET: Physics, Instrumentation, and Scanners,* New York: Springer Science+Business Media, 2006.

7. Annihilation phenomenon. Available: http://www.internaldosimetry.com/courses/introdosimetry/images/Annihilation.JPG.

8. National Electrical Manufacturers Association, *NEMA Standards Publication NU 2-2001 Performance Measurements of Positron Emission Tomographs,* 2001.

9. Knoll, G. F., *Radiation Detection and Measurement*, New York: John Wiley & Sons, 3rd ed., 2000.

10. Doshi, N. K., Y. Shao, R. W. Silverman and S. R. Cherry, "Design and Evaluation of an LSO PET Detector for Breast Cancer Imaging," *Med Phys*, Vol. 27(7), pp. 1535-1543, July 2000.

11. Photomultiplier tube. Available: http://www.physics.ubc.ca/~mirg/home/tutorial/pics/pmt.gif.

12. Cross-section of a PD. Available: http://sales.hamamatsu.com/assets/html/ssd/si-photodiode/images/characteristic/03_01.gif.

13. Block PMT assembly. Available: https://petcenter.hsc.usc.edu/USC_Site/images/scientific/instruments/blockPMTassembly.jpg.

14. Schematic of the quadrant-sharing detector design. Available: http://www.mdanderson.org/images/pet_quad_pqsdesign.jpg.

15. Bronstein, A, M. Bronstein, M. Zibulevsky and Y. Y. Zeevi, "High-Energy Photon Detection in Positron Emission Tomography using Adaptive Non-linear Parametric Estimation Algorithms," preprint, Israel Institute of Technology, Haifa, Israel, 2002.

16. Vaska, P., M. J. Petrillo and G. Muehllehner, "Virtual PMTs: Improving Centroid Positioning Performance Near the Edges of a Gamma Camera Detector," *IEEE Trans Nucl Sci*, Vol. 48(3), pp. 645-649, June 2001.

17. Gagnon, D., N. Pouliot, L. Laperriere, M. Therrien and P. Olivier, "Maximum Likelihood Positioning in the Scintillation Camera Using Depth of Interaction," *IEEE Trans Med Imag*, Vol. 12(1), pp. 101-107, March 1993.

18. Joung, J., R. S. Miyaoka, S. Kohlmyer and T. K. Lewellen, "Implementation of ML Based Positioning Algorithms for Scintillation Cameras," *IEEE Trans Nucl Sci*, Vol. 47(3), pp. 1104-1111, June 2000.

19. Joung, J., S. Miyaoka, S. G. Kohlmyer and T. K. Lewellen, "Investigation of Bias-Free Positioning Estimators for the Scintillation Cameras," *IEEE Trans Nucl Sci*, Vol. 48(3), pp. 715-719, June 2001.

20. Chung, Y. H., Y. Choi, T. Y. Song, J. H. Jung and G. Cho, "Evaluation of Maximum-Likelihood Position Estimation with Poisson and Gaussian Noise Models in a Small Gamma Camera," IEEE Trans Nucl Sci, Vol. 51(1), pp. 101-104, 2004.

21. Ling, T., K. Lee and R. S. Miyaoka, "Performance Comparisons of Continuous Miniature Crystal Element (cMice) Detectors," *IEEE Trans Nucl Sci*, Vol. 53(5), pp. 2513-2518, October 2006.

22. Berk, S., "Design Optimization of a Continuous Detector for PEM Imaging with High Resolution and DOI Capability," Master's thesis, Boğaziçi University, Istanbul, Turkey, 2006.

23. Dokhale, P. A., R. W. Silvermann, K. S. Shah, R. Grazioso, R. Farrell, J. Glodo, M. A. McClish, G. Entine, V-H Tran and S. R. Cherry, "Performance Measurements of a Depth-Encoding PET Detector Module Based on Position-Sensitive Avalanche Photodiode Read-Out," *Phys Med Biol*, Vol. 49, pp. 4293-4304, Sept 2004.

24. Bronstein, A., M. Bronstein, M. Zibulevsky and Y. Y. Zeevi, "Optimal Nonlinear Line-of-Flight Estimation in Positron Emission Tomography," *IEEE Trans. Med. Imag.*, Vol. 50, pp. 421-426, Jun 2002.

25. Aliaga, R. J., J. D. Martinez, R. Gadea, A. Sebastia, J. M. Benlloch, F. Sanchez, N. Pavon and Ch. Lerche, "Corrected Position Estimation in PET Detector Modules with Multi-Anode PMTs Using Neural Networks," *IEEE Trans Nucl Sci*, Vol. 53(3), pp. 776-783, June 2006.

26. Thompson, C. J., K. Murthy, I. N. Weinberg and F. Mako, "Feasibility for Positron Emission Mammography," *Med Phys*, Vol. 21(4), pp. 529-538, April 1994.

27. Thompson, C. J., K. Murthy, Y. Picard, I. N. Weinberg and R. Mako, "Positron Emission Mammography (PEM): A Promising Technique for Detecting Breast Cancer," *IEEE Trans Nucl Sci*, Vol. 42(4), pp. 1012-1017, Aug 1995.

28. Thompson, C. J., K. Murthy, R. L. Clancy, J. L. Robar, A. Bergman, R. Lisbona, A. Loutfi, J. H. Gagnon, I. N. Weinberg and R. Mako, "Imaging Performance of PEM-1: A High Resolution System for Positron Emission Mammography," *IEEE Nucl Sci Symp and Med Imag Conf Rec*, Vol. 2, pp. 1074-1078, 21-28 Oct 1995.

29. Murthy, K., M. Aznar, A. M. Bergman, C. J. Thompson, J. L. Robar, R. Lisbona, A. Loutfi and J. H. Gagnon, "Positron Emission Mammographic Instrument: Initial Results," *Radiology*, Vol. 215, pp. 280-285, 2000.

30. Murthy, K., M. Aznar, C. J. Thompson, A. Loutfi, R. Lisbona and J. H. Gagnon, "Results of Preliminary Clinical Trials of the Positron Emission Mammography System PEM-I: A Dedicated Breast Imaging System Producing Glucose Metabolic ImagesUsing FDG," *J Nucl Med*, Vol. 41, pp. 1851-1858, 2000.

31. Moses, W. W., T. F. Budinger, R. H. Huesman and S. E. Derenzo, "PET Camera Designsfor Imaging Breast Cancer and Axillary Node Involvement (Abstract)," *J Nucl Med*, Vol. 36, pp. 69P, 1995.

32. Virador, P. R. G., W. W. Moses and R. H. Huesman, "Reconstruction in PET Cameras with Irregular Sampling and Depth of Interaction Capability," *IEEE Trans Nucl Sci*, Vol. 45(3), pp. 1225-1230, June 1998.

33. Virador, P. R. G., W. W. Moses and R. H. Huesman, "3D Reconstruction in PET Cameras with Irregular Sampling and Depth of Interaction," *IEEE Trans Nucl Sci*, NS-48, pp. 1524-1529, 2001.

34. Weinberg, I., S. Majewski, A. Weisenberger, A. Markowitz, L. Aloj, L. Majewski, D. Danforth, J. Mulshine, K. Cowan, J. Zujewski, C. Chow, E. Jones, V. Chang, W. Berg and J. Frank, "Preliminary Results for Positron Emission Mammography: Real-Time Functional Breast Imaging in a Conventional Mammography Gantry," *Eur J Nucl Med*, Vol. 23(7), pp. 804-806, July 1996.

35. Weinberg, I. N., P. Y. Stepanov, D. Beylin, V. Zavarzin, E. Anashkin, K. Lauckner, S. Yarnall, M. Doss, R. Pani and L. P. Adler, "PEM-2400 – A Biopsy-Ready PEM Scanner with Real-Time X-Ray Correlation Capability," *IEEE Nucl Sci Symp Conf Rec*, Vol. 2, pp. 1128-1130, 10-16 Nov 2002.

36. Frelfelder, R. and J. S. Karp, "Dedicated PET Scanners for Breast Imaging," *Phys Med Biol*, Vol. 42, pp. 2463-2480, 1997.

37. Freifelder, R., C. Cardi, I. Grigoras, J. R. Saffer and J. S. Karp, "First Results of a Dedicated Breast PET Imager, BPET, Using NaI(Tl) Curve Plate Detectors," *IEEE Nucl Sci Sym Conf Rec*, Vol. 3, pp. 1241-1245, 4-10 Nov 2001.

38. Raylman, R. R., S. Majewski, R. Wojcik, A. G. Weisenberger, B. Kross and H. Bishop, "The Potential Role of Positron Emission Mammography for Detection of Breast Cancer. A Phantom Study," *Med Phys*, Vol. 27(8), pp. 1943-1954, Aug 2000.

39. Smith, M. F., R. R. Raylman, S. Majewski and A. G. Weisenberger, "Positron Emission Mammography with Tomographic Acquisition Using Dual Planar Detectors: Initial Evaluations," *Phys Med Biol*, Vol. 49, pp. 2437-2452, 2004.

40. Doshi, N. K., R. W. Silvermann, Y. Shao and S. R. Cherry, "maxPET: A Dedicated Mammary and Axillary Region PET Imaging System for Breast Cancer," *IEEE Trans Nucl Sci*, Vol. 48(3), pp. 811-815, June 2001.

41. Lecoq, P. and J. Varela, "Clear-PEM, a Dedicated PET Camera for Mammography," *Nucl Inst Meth Phys Res A*, Vol. 486, pp. 1-6, 2002.

42. Ribeiro, R., C. Abreu, P. Almeida, F. Balau, P. Bordalo, N. C. Ferreira, S. Fetal, F. Fraga, P. Lecoq, M. Martins, N. Matela, R. Moura, C. Ortigao, L. Peralta, S. Ramos, P. Rato, P. Rodrigues, A. I. Santos, A. Trindade and J. Varela, "Breast Imaging with a Dedicated PEM," *Nucl Ins Meth Phys Res A*, Vol. 527, pp. 87-91, 2004.

43. Abreu, M., J. D. Aguiar, F. G. Almeida, P. Almeida, P. Bento, B. Carriço, M. Ferreira, N. C. Ferreira, F. Gonçalves, C. Leong, F. Lopes, P. Lousa, M. V. Martins, N. Matela, P. R. Mendes, R. Moura, J. Nobre, N. Oliveira, C. Ortigao, L. Peralta, R. Pereira, J. Rego, R. Ribeiro, P. Rodrigues, J. Sampaio, A. I. Santos, L. Silva, J. C. Silva, P. Sousa, I. C. Teixeira, J. P. Teixeira, A. Trindade and J. Varela, "Design and Evaluation of the Clear-PEM Scanner for Positron Emission Mammography," *IEEE Trans Nucl Sci*, Vol. 53(1), pp. 71-77, Feb 2006.

44. Adler, L. P., I. N. Weinberg, M. S. Bradbury, E. A. Levine, N. M. Lesko, K. R. Geisinger, W. A. Berg and R. I. Freimanis, "Method for Combined FDG-PET and Radiographic Imaging of Primary Breast Cancers," *The Breast Journal*, Vol. 9(3), pp. 163-166, 2003.

45. Levine, E. A., R. I. Freimanis, N. D. Perrier, K. Morton, N. M. Lesko, S. Bergman, K. R. Geisinger, R. C. Williams, C. Sharpe, V. Zavarsin, I. N. Weinberg, P. Y. Stepanov, D. Beylin, K. Lauckner, M. Doss, J. Lovelace and L. P. Adler, "Positron Emission Mammography: Initial Clinical Results," *Ann Surg Oncol*, Vol. 10(1), pp. 86-91, 2003.

46. Del Guerra, A., N. Belcari, W. Bencivelli, A. Motta, S. Righi, A. Vaiano, G. Di Domenico, E. Moretti, N. Sabba, G. Zavattini, R. Campanini, N. Lanconelli, A. Riccardi, M. N. Cinti, R. Pani and R. Pellegrini, "Monte Carlo Study and Experimental Measurements of Breast Tumor Detectability with the YAP-PEM Prototype," *IEEE Nucl Sci Symp Conf Rec*, Vol. 3, pp. 1887-1891, 10-16 Nov 2002.

47. Motta, A., S. Righi, A. Del Guerra, N. Belcari, A. Vaiano, G. Di Domenico, G. Zavattini, R. Campanini, N. Lanconelli and A. Riccardi, "A Full Monte Carlo Simulation of the YAP-PEM Prototype for Breast Tumor Detection," *Nucl Ins Meth Phys Res A*, Vol. 527, pp. 201-205, 2004.

48. Belcari, N., M. Camarda, A. Del Guerra, D. Herbert, A. Motta, A. Vaiano, G. Di Domenico and G. Zavattini, "Development of a Planar Head PEM System Based on an Array of PSPMT and YAP Crystals," *IEEE Nucl Sci Symp Conf Rec*, Vol. 3, pp. 2179-2182, 19-25 Oct 2003.

49. Karimian, A., C. J. Thompson, S. Sarkar, G. Raisali, R. Pani, H. Davilu and D. Sardari, "A Dedicated PET System for Breast Imaging (CYBPET)," *IEEE Nucl Sci Symp Conf Rec*, Vol. 4, pp. 2339-2341, 16-22 Oct 2004.

50. Karimian, A., C. J. Thompson, S. Sarkar, G. Raisali, R. Pani, H. Davilu and D. Sardari, "CYBPET: A Cylindrical PET System for Breast Imaging," *Nucl Ins Meth Phys Res A*, Vol. 545, pp. 427-435, 2005.

51. Hoskinson, E. and C. Moisan, *The GRIT Essentials, TRIUMF 4004, Version 3.0*, User's manual, Laval University, Quebec, Canada, May 1995.

52. Moisan, C. and G. McDonald, *BUILDER – A High Level Language Interface to DETECT for the Design of Scintillation Detectors, Version 6.0*, User's manual, Laval University, Quebec, Canada, Sep 2000.

53. Moisan, C., F. Cayouet and G. McDonald, *DETECT2000 - The Object Oriented C++ Language Version of DETECT, A Program for Modeling Optical Properties of Scintillators, Version 5.0*, User's manual, Laval University, Quebec, Canada, Sep 2000.

54. Haykin, S., Neural Networks, New Jersey: Prentice-Hall, 2nd ed., 1999.

55. Hamamatsu H8500 Flat Panel Multi-Anode PMT Specification Sheet. Available: http://jp.hamamatsu.com/resources/products/etd/pdf/H8500_H8500B_TPMH1282E09.pdf.

56. Izenman, A. J., "Recent Developments in Nonparametric Density Estimation," *JASA*, Vol. 86(413), pp. 205-224, Mar 1991.

57. Seidel, J., W.R. Gandler and M. V. Green, "Characteristics of a Pair of Small Field-of-View LSO Scintillation Cameras", *IEEE Trans Nucl Sci*, Vol. 43(3), pp. 1968-1973, June 1996.